UNIVERSITY OF CALIFORNIA,
IRVINE

Using Molecular States to Probe Spin Properties of Single Molecules

THESIS

Submitted in partial satisfaction of the requirements
For the degree of

MASTER OF SCIENCE
in Physics

by

Peter John Wagner

Dissertation Committee:
Professor Wilson Ho, Chair
Professor Ruqian Wu
Professor Zuzanna Siwy

2021

DEDICATION

To my friends and family

TABLE OF CONTENTS

LIST OF FIGURES

LIST OF TABLES

ACKNOWLEDGEMENTS

First, I must thank Wilson Ho, my graduate advisor. Without his guidance, advice, and mentorship, none of this work would have been possible. I also thank my PhD Dissertation Committee members, Prof. Ruqian Wu and Prof. Zuzanna Siwy, along with my Advancement Committee members Prof. Kumar Wickramasinge and Prof. Ilya Krivorotov.

I also must thank my mK-STM partners, Dr. Greg Czap, Jiang Yao, Yunpeng Xia and Wenlu Shi, who worked with me when running these experiments and provided valuable discussions about the meaning behind the data.

My former group members who mentored me also deserve my gratitude. Dr. Calvin Patel and Dr. Shaowei Li were instrumental in my development as a scientist. I also thank the Ho group members with whom I spent so much time, Christian Kim, Likun Wang, Siyu Chen, Dr. Youngwook Park and Dr. Irving Caballerro-Quintana for their support.

I must also thank our collaborators Jie Li, Feng Xue, and Lei Gu in Prof. Ruqian Wu's group and Brian Nguyen in Prof. Filipp Furche's group who worked hard on the computer calculations to support our experimental results.

Kevin Tkaczibson of Shane Ardo's group also has my gratitude for his assistance in the preparation of the dosing apparatus needed for the experiments discussed in this thesis.

Without the love and support of my friends and family, I admit that I would have given up long ago. Thank you for everything.

Lastly, I want to thank the sources of funding that made this research possible:

Chemical Science, Geo- and Bioscience Division, Office of Science, U.S. Department of Energy, under Grant No. DE-FG02-04ER15595

Office of Naval Research under Grant No. N00014-20-1-2475

National Science Foundation under Grant No. DMR-1809127

CURRICULUM VITAE

Peter Wagner

Education

SEPTEMBER 2021
PHD IN PHYSICS, UNIVERSITY OF CALIFORNIA, IRVINE
GPA: 3.90 Chemical and Material Physics Interdisciplinary PhD program

JUNE 2012
BS IN PHYSICS, UNIVERSITY OF CALIFORNIA, DAVIS
GPA: 3.49 Coursework emphasis on Condensed Matter Physics

Technical Skills

- Familiar with standard machine shop tools: Milling tree, Lathe, Bandsaw, Belt Sander
- Programming Languages and Tools: C, C++, Java, Python, Mathematica, LabVIEW, Code Composer Studio
- Data Processing and Presentation Software: Adobe Photoshop, Adobe Illustrator, Autodesk Inventor, Autodesk AutoCAD, LaTeX, Origin

Publications

- Z. Feng, A. Mazaheripour, D. J. Dibble, **P. Wagner**, G. Czap, G. Kladnik, A. Cossaro, A. Verdini, L. Floreano, G. Bavdek, W. Ho, G. Comelli, D. Cvetko, A. Morgante, and A. A. Gorodetsky, Bottom-up Synthesis of Nitrogen-Containing Graphene Nanoribbons from the Tetrabenzopentacene Molecular Motif, Carbon **170**, 677-684 (2020).
- G. Czap, **P. J. Wagner**, J. Li, F. Xue, J. Yao, R. Wu, W. Ho , Detection of Spin-Vibration States in Single Magnetic Molecules. *Phys. Rev. Lett.* **123**, 106803-1–6 (2019).
- G. Czap, **P. J. Wagner**, F. Xue, L. Gu, J. Li, J. Yao, R. Wu, W. Ho, Probing and imaging spin interactions with a magnetic single-molecule sensor. *Science* **364**, 670–673 (2019).
- G. Czap, Z. Han, **P. J. Wagner**, W. Ho, Detection and Characterization of Anharmonic Overtone Vibrations of Single Molecules on a Metal Surface. *Phys. Rev. Lett.* **122**, 106801-1–5 (2019).
- Z. Han. G. Czap, C. L. Chiang, C. Xu, **P. J. Wagner**, X. Wei, Y. Zhang, R. Wu, W. Ho, Imaging the halogen bond in self-assembled halogenbenzenes on silver. *Science.* **358**, 206–210 (2017).

Honors

- UC Davis Regents Scholar: 2009 – 2012
- UC Davis Dean's Honors List: Spring 2009, Fall 2009, Fall 2010

THESIS ABSTRACT

Using Molecular States to Probe Spin Properties of Single Molecules

By

Peter John Wagner

Master of Science in Physics

University of California, Irvine, 2021

Professor Wilson Ho, Chair

Here, we discuss the enhancement of the scanning tunneling microscope (STM) through the functionalization of the STM tip with single molecules. Using a sub-Kelvin STM, we observe that a magnetic molecule can be reproducibly transferred from the surface to the tip and forms a Kondo state. This many-body resonance undergoes exchange splitting in the proximity of another magnetic molecule adsorbed on the substrate surface and exhibits effects of spin polarization in the mutual inelastic conductance. The Kondo tip influences the inelastic spin-flip excitation in the magnetic molecule and a hybrid Kondo-spin excitation state emerges. These results reveal magnetic sensing between a many-body resonance and discrete excitations between two magnetic molecules.

CHAPTER 1

Introduction

1.1 Scanning Tunneling Microscopy

Scanning Tunneling Microscopy as a technique has been developed significantly since its inception in 1982 by Binnig and Rohrer. The first successful experiment with a scanning tunneling microscope demonstrated that the device could consistently control the tunneling gap and show that the tunneling current depends exponentially on the total gap distance [1]. Not long after, Au(110) and Si(111) surfaces were mapped with a lateral resolution of a few Å, revealing monoatomic steps along the surface [2,3].

To achieve this "unprecedented resolution," the first microscope used piezodrives to move a tungsten field emission microscopy tip with a tip radius on the order of 100 Å [3]. While the tip is not atomically sharp, thanks to the tunneling current's exponential dependence on the gap, the tip atom closest to the surface contributes most of the current. The macroscopic sharpness of the tip helps by reducing the number of atoms of similar distance to the surface. Between the antenna-like shape of the tip and requirement for the tunneling gap to be stable, layers of vibration damping are needed. The first scanner was mounted on an air-supported stone bench and floated using a superconducting lead bowl over strong permanent magnets [1].

For all the experiments discussed in this dissertation, we use a home-built Besocke-style STM scanner [4]. Shown in Fig. 1.1A, the STM tip is positioned below the sample crystal in a piezoelectric tube and only moves vertically. Three other piezotubes topped with tungsten balls support the sample holder, moving the sample laterally and vertically relative to the tip. The sample crystal is mounted in the center of the molybdenum sample holder with circularly

symmetric ramps, seen in Fig. 1.1C. The ramps allow the three outer piezotubes to bring the sample crystal closer to the tip without applying a bias to the tip piezo.

The scanner is connected by springs to a long manipulator arm able to move the scanner between an access position and an experiment position. Additionally, a copper rod is mounted to the bottom of the scanner positioned in the center of an array of permanent magnets to act as a vibrational damper. The entire apparatus is mounted on a heavy optical table floated by nitrogen vibration damping legs at each corner.

Control of the biases applied to the scanner is handled by a digital signal processor (DSP) to avoid any interruptions from any peripheral software running on the data acquisition computer (see Fig. 1.2). To remove the electronic noise coming from the DSP to the STM scanner, all commands from the DSP first pass through an opto-isolator. After going through the opto-isolator, the digital signal is converted to an analog voltage and sent to one of eight channels to control the motion of the scanner piezos. The tunneling current must pass through a pre-amplifier before being processed by the electronics. The tunneling current signal is sent through a feedback loop that controls the bias of the center piezotube, maintaining a fixed tunneling gap by matching the measured tunneling current to a set point current. Finally, the tunneling current signal and the feedback bias are converted back to a digital signal to be read by the DSP.

The primary physical principle of the STM is the quantum tunneling of electrons. The tunneling current between the STM tip and sample is determined by the distance between the tip and surface, the voltage applied between the tip and surface, and the electronic states of the tip and surface. The tunneling current J_T can be expressed to first order as $J_T \propto V_T \exp(-A\,\varphi^{1/2} s)$, where V_T is the sample-tip bias voltage, ϕ is the work function, and s is the distance between the tip and sample. In practice, a change of one angstrom in the tip-sample distance changes the

tunneling current by an order of magnitude. To maintain a fixed tunneling gap, the tunneling current is compared to a setpoint current in a negative feedback loop that outputs voltage to the center piezotube.

In general, we use two different scanning pathways when taking images of the sample crystal shown in Fig. 1.3. The simpler pathway holds the central piezo still while the sample moves laterally, raster scanning over the surface and mapping the resulting tunneling current. This method is called Constant Height since the tip height is held constant during the scan. The other pathway uses the feedback circuit to maintain a constant tunneling current during tip motion, mapping the applied center piezo bias instead of the tunneling current. As this method holds the tunneling current fixed, this pathway is called Constant Current.

1.2 Inelastic Electron Tunneling Spectroscopy

When a molecule or atom is introduced into the tunneling junction, characterizing the tunneling current becomes more complex. Often the system is modeled as a two tunneling barriers separating the tip from the molecule and the molecule from the surface (see Fig. 1.4). Other than the change to the tunneling barriers, the molecule includes inelastic transitions representing vibrational, rotation, electronic and spin excitations as different energy levels the tunneling electron can lose energy to.

Tunneling current can be split into contributions from elastic channels and inelastic channels. In many cases, the elastic channels dominate the tunneling current, but the inelastic channels reveal more information about the system in the tunneling junction. Inelastic electron tunneling spectroscopy can identify various transitions that can occur in molecular and atomic systems, such as vibrational [5], rotational or spin flip excitations. The technique can also show resonant tunneling, such as Kondo resonance, as a peak in the conductance [6,7].

The signal from inelastic transitions appears as a step in the conductance in the tunneling gap as the energy of the electron matches the inelastic excitation energy. The transition can be seen as a kink in the I-V curve, a step in the first derivative and as a peak in the second derivative. A lock-in amplifier is used to extract this information by applying an AC bias between the tip and sample and measuring the first and second harmonic of the I-V curve taken over the system in question. Using a simple sinusoidal wave for the lock-in bias and a Taylor series to approximate the resulting tunneling current, we get the following expression:

$$I_T(V_0 + V_{AC}\cos(\omega t)) = I_T(V_0) + \left.\frac{\partial I}{\partial V}\right|_{V_0} V_{AC}\cos(\omega t) + \left.\frac{1}{2}\frac{\partial^2 I}{\partial V^2}\right|_{V_0} {V_{AC}}^2\cos(\omega t)^2 + O({V_{AC}}^3)$$

where I_T is the tunneling current as a function of sample bias, V_0 is the DC sample bias, V_{AC} is the amplitude of the lock-in bias, and ω is the frequency of the sinusoidal wave. A trigonometric identity changes the expression to

$$I_T(V_0 + V_{AC}\cos(\omega t)) = I_T(V_0) + \left.\frac{1}{4}\frac{\partial^2 I}{\partial V^2}\right|_{V_0} {V_{AC}}^2 + \left.\frac{\partial I}{\partial V}\right|_{V_0} V_{AC}\cos(\omega t) + \left.\frac{1}{4}\frac{\partial^2 I}{\partial V^2}\right|_{V_0} {V_{AC}}^2\cos(2\omega t) + O({V_{AC}}^3)$$

. From this expression, we can extract the first derivative from the first harmonic and the second derivative from the second harmonic. The error from this approximation is small as long as the amplitude of the lock-in bias is kept small. The first derivative reduces the contribution of any elastic channels to a constant offset added to the spectra while the second derivative removes the elastic contributions entirely.

One of the advantages of IETS is the high energy resolution for detecting inelastic transitions. The energy resolution is controlled by the temperature of the tunneling junction, the instrumental broadening introduced by the lock-in amplifier, and any intrinsic width of a given

inelastic excitation. In the approximation that each of these contributions to the peak width has a Gaussian distribution, we can add the squares of each effect to get the resulting peak width. Lauhon and Ho measured the temperature and modulation dependence of the line width of the C-H stretch peak of acetylene on Cu(100) [8]. The resulting fit gives the following equation for the line width of an inelastic peak.

$$W = \sqrt{W_I^2 + (1.7\,V_{AC})^2 + (5.4\,k_B T/e)^2}$$

Temperature broadening is a consequence of the electrons obeying Fermi-Dirac statistics. At higher temperatures, the distribution of electron energy is broader meaning that electrons will start tunneling into an inelastic channel over a larger sample-tip bias range.

The lock-in amplifier introduces a modulation voltage into the tunneling junction to measure the first and second derivative of the I-V curve. The measurement of these curves is a convolution of derivative curve and an instrumental function that can be determined by the exact details of the modulation voltage [9]. For a sinusoidal modulation with an rms amplitude of V_{mod}, the instrumental function can be approximated by a normal distribution with a width of ~1.7 V_{mod} [8,9].

The intrinsic width is less well defined for different inelastic excitations. For the hindered rotation excitation of CO on Cu(100), the intrinsic width is reported to be 6±2 meV [10], but for the C-C stretch mode in an alkanedithiol monolayer is reported as 3.73±0.98 meV [11]. In contrast, the width of the spin flip excitation of nickelocene on Cu(100) is only ~1 meV [12]. Galperin et al. conclude that the coupling of the vibrational motion of a molecule with the conduction electrons of the lead to which it is most strongly bound contributes to the intrinsic linewidth of inelastic transitions [6]. For spin impurities, the Kondo resonance in the first derivative has an intrinsic width that depends on its Kondo temperature [13].

1.3 Inelastic Tunneling Probe

One of the major strengths of combining IETS with STM is the spatial and energy resolution. By using a lock-in amplifier to read the dI/dV and d^2I/dV^2 signal at a fixed bias, we can measure the energy and intensity shifts of a single inelastic transition mapped over an area. This technique, called itProbe, can reveal different features about the system being imaged depending on the transition that is measured.

When using a sharp, bare tip, the inelastic channels available for electrons to tunnel into are constrained by the system being imaged on the surface. By imaging a bias that corresponds to one of these inelastic transitions, we learn the positions over the molecule where the excitation is the strongest. For example, by setting the bias to the energy of the first positive bias electronic excitation, the LUMO of the system is imaged. This technique gives submolecular resolution of the features of the systems studied but improved resolution can be achieved by introducing another molecule onto the STM tip.

By picking up single molecules from the sample surface to the STM tip, the resolution of the topography can be improved by effectively sharpening the tip, depending on the molecule adsorbed, to a single atom apex. Simple molecules like CO and C_2H_4 have been tested as tip apex molecules and have shown improved topographical resolution to the point of identifying the atomic lattice of a crystal surface. [14] With CO on the tip, we get improved topographical resolution and an inelastic transition that is sensitive to the environment of the tip. The hindered translation (HT) vibration mode of a CO molecule is red-shifted when positioned over the repulsive potential of atoms or bonds of a molecule as shown in Fig. 1.5. By imaging the positions where the HT mode of the CO tip is reduced in energy, we reveal structural information about molecules on the surface [15,16].

While simple molecules are preferred for vibrational itProbe, we find that nickelocene has a spin sensitive excitation useful for probing molecular systems. Nickelocene's five-member carbon rings isolate the d-orbital electrons from the conductive STM tip and surface, making the molecule a suitable spin-flip excitation probe. [17] The $M_s = 0$ to $M_s = \pm 1$ transitions have a magnetic anisotropy energy of ~3.8 mV and the degenerate transitions are split by an external magnetic field and spin exchange splitting. [12] By observing the energy shifts of nickelocene's spin flip transitions due to the surface system, we learn about the strength of the exchange coupling between the probe molecule and the target surface.

1.4 mK-STM Overview

In this dissertation, we use a homebuilt ultrahigh-vacuum STM capable of reaching 0.5 K with a uniaxial superconducting magnet able to apply a +/- 9 Tesla magnetic field on the single crystal metal surface. We can cool the scanner down to sub-Kelvin temperatures for approximately 48 hours at a time using a one-shot closed-cycle liquid helium-3 refrigerator. To achieve those temperatures, we first release the ^{3}He gas from the charcoal pump by heating it in the closed-cycle system. ^{3}He has a boiling point of 3.2 K, so we cool the gas by pumping on liquid ^{4}He, cooling a small reservoir called the 1K pot and condensing the ^{3}He gas. Once enough liquid ^{3}He has accumulated, the charcoal pump is cooled back down and allowed to pump on the liquid ^{3}He, further reducing the temperature of the scanner down to ~0.5 K. Further details about the design, construction and operation of the cryostat for our scanner are outlined in the theses of Drs. Xi Chen [18], Ungdon Ham [19], and Chi-Lun Jiang [20].

1.5 Summary of Contents

In Chapter 2 “Spin Dependent Tunneling,” the effect of cobaltocene as a magnetic impurity in the STM junction is explored. The interactions between cobaltocene and nickelocene reveal the nature of the spin-dependent tunneling in the junction.

In the concluding chapter, we summarize the work presented and suggest further experiments and projects to be explored in the future.

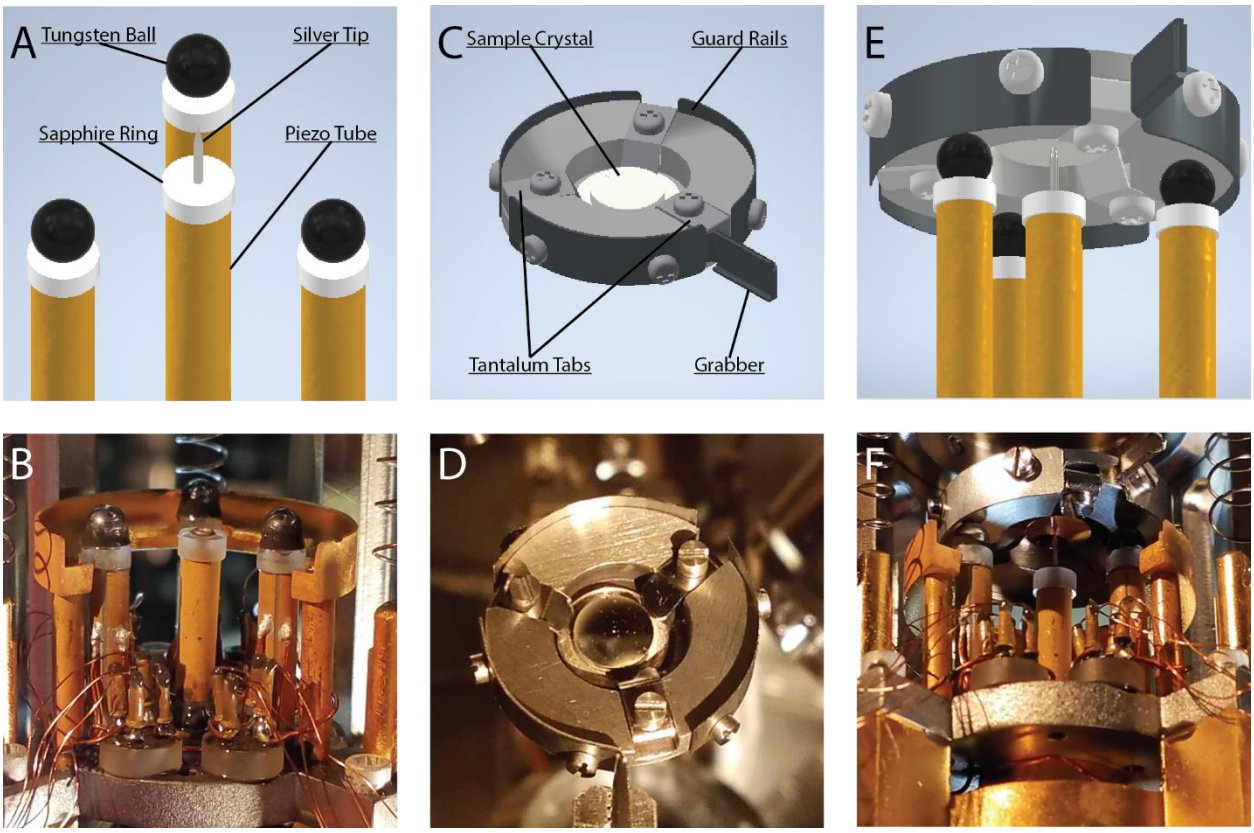

Figure 1.1: Besocke-style STM Scanner and Sample Holder

Components of a Besocke-style STM scanner. Schematic (A) and picture (B) of piezo elements of the STM scanner. Silver STM tip is absent from the center piezo in (B). Schematic (C) and picture (D) of sample holder for Ag(110) crystal. Schematic (E) and picture (F) of fully assembled Besocke STM scanner.

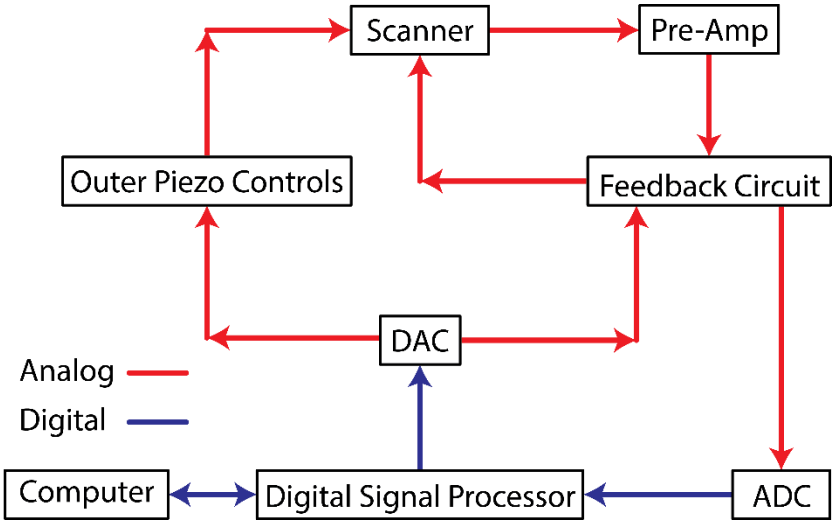

Figure 1.2: Schematic of the electronic connections controlling the STM scanner

Digital and analog signal circuits for communication between the data acquisition computer and the STM scanner. Digital communication is handled by the digital signal processor sending commands through the DAC and receiving data from the ADC. New outputs can be sent directly to the scanner piezos or to the feedback circuit maintaining the tunneling gap between the tip and sample.

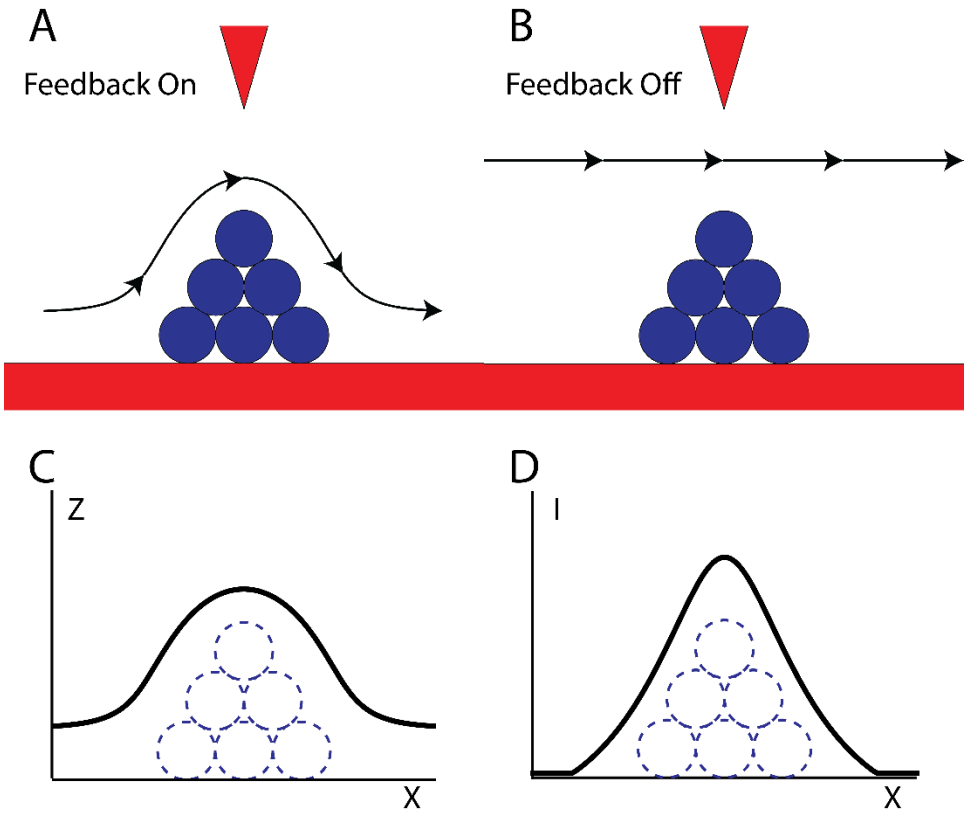

Figure 1.3: Constant Height and Constant Current Scanning Paths

Constant current (A) and constant height (B) scanning pathways the tip takes when moving over an object on the substrate. The resulting measurements for a line scanned in constant current (C) mode and constant height (D) mode.

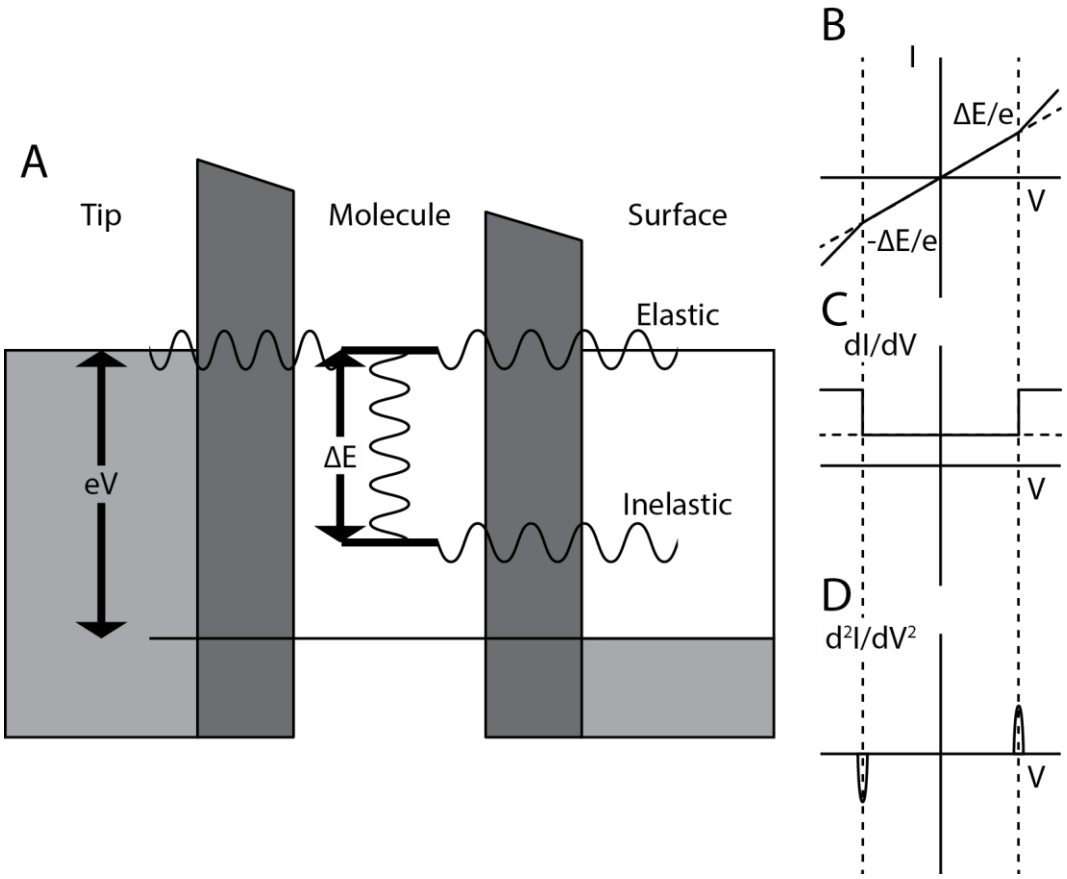

Figure 1.4: Elastic and Inelastic Tunneling

Schematic of a double barrier tunneling junction. (A) Example elastic and inelastic channels shown tunneling through two state system in STM junction. I-V (B), *dI/dV* (C), and d^2I/dV^2 (D) curves for example two state system.

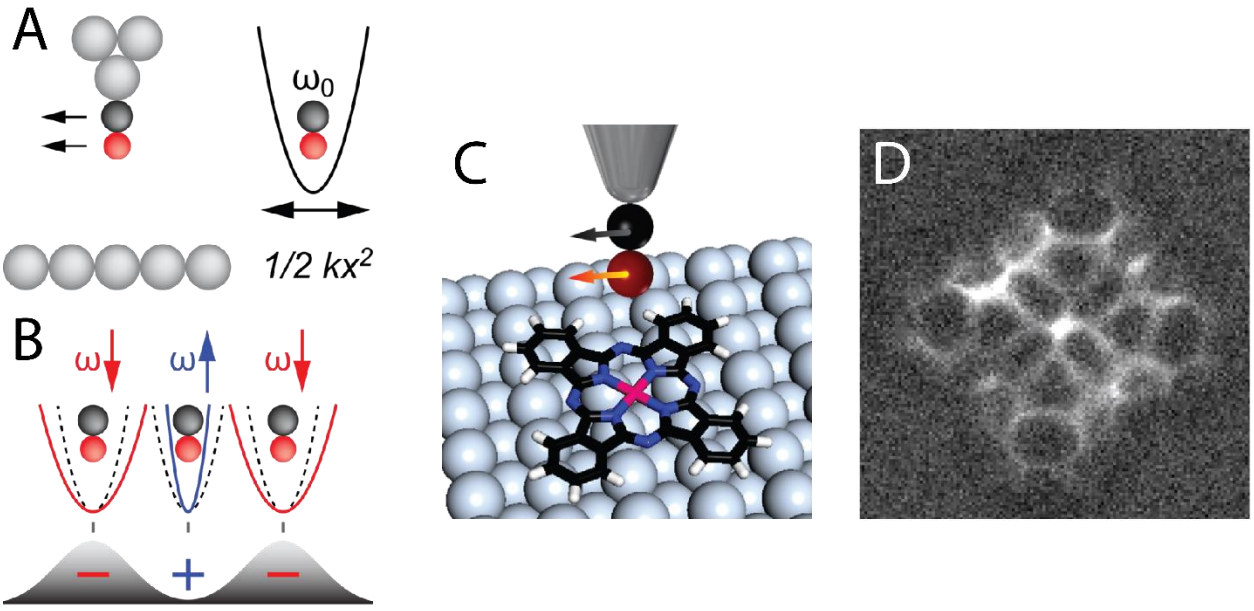

Figure 1.5: itProbe Structure Mapping

(A) Schematic of a CO molecule attached to the STM tip. The hindered translation (HT) vibration mode is approximated as a quantum harmonic oscillator with a stiffness k determined by the STM tip and the local environment on the surface, giving an energy difference of $\hbar\omega_0$. (B) Diagram showing the effect of the repulsive ridges and attractive wells on the CO HT vibrational mode energy. (C) Schematic of the tunneling gap with CO attached to the tip and a cobalt phthalocyanine molecule adsorbed on the Ag(110) terrace. (D) itProbe image of cobalt phthalocyanine taken with CO tip, mapping the softening of the HT mode.

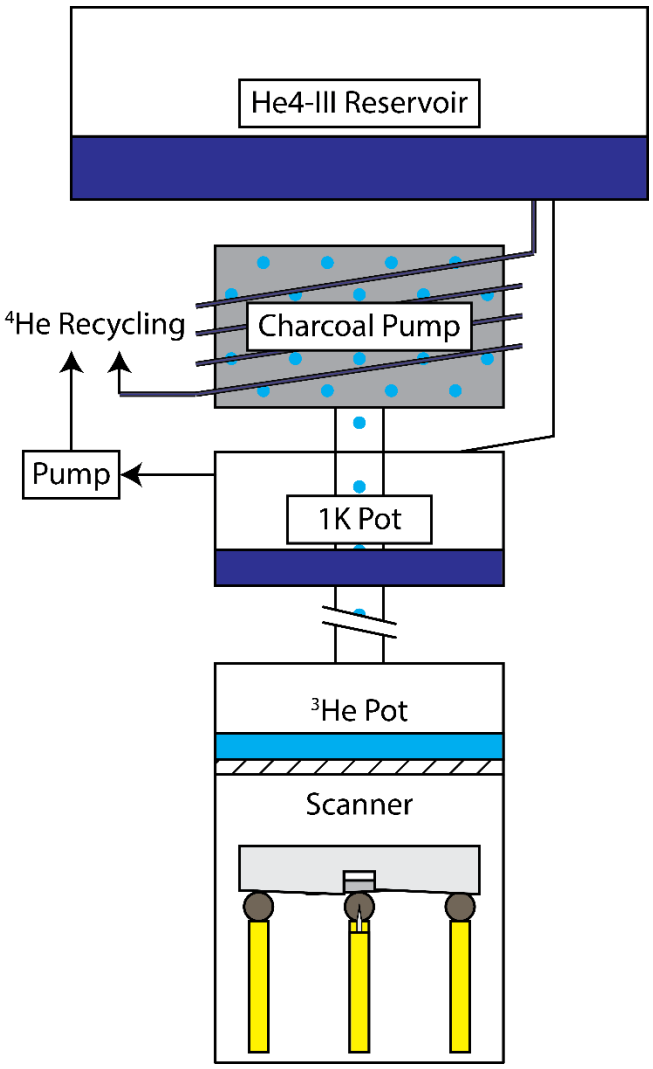

Figure 1.6: Sub-Kelvin ^{3}He Liquefication System

Schematic of the ^{3}He liquefication components of the sub-Kelvin STM. The He4-III reservoir maintains the liquid helium level in the 1K pot and provides external cooling for the charcoal pump. During liquefication, the 1K pot is pumped on, lowering the boiling point of ^{4}He (dark blue) to ~1.4K which is below the boiling point of ^{3}He (light blue) in ambient conditions. By applying heat to the charcoal pump, the ^{3}He gas is released and exposed to the cold surface of the 1K pot, causing the liquid ^{3}He to accumulate in the ^{3}He pot.

References

[1] G. Binnig, H. Rohrer, C. Gerber, and E. Weibel, *Tunneling through a Controllable Vacuum Gap*, Appl. Phys. Lett. **40**, 178 (1982).

[2] G. Binnig and H. Rohrer, *Scanning Tunneling Microscopy*, Surf. Sci. **126**, 236 (1982).

[3] G. Binnig, H. Rohrer, C. Gerber, and E. Weibel, *Surface Studies by Scanning Tunneling Microscopy*, Phys. Rev. Lett. **49**, 57 (1982).

[4] K. Besocke, *An Easily Operable Scanning Tunneling Microscope*, Surf. Sci. **181**, 145 (1987).

[5] W. Ho, *Single-Molecule Chemistry*, J. Chem. Phys. **117**, 11033 (2002).

[6] M. Galperin, M. A. Ratner, and A. Nitzan, *Inelastic Electron Tunneling Spectroscopy in Molecular Junctions: Peaks and Dips*, J. Chem. Phys. **121**, 11965 (2004).

[7] B. N. J. Persson, A. Baratoff, B. N. J. Persson, and A. Baratoff, *Inelastic Electron Tunneling from a Metal Tip: The Contribution from Resonant Processes*, Phys. Rev. Lett. **59**, 339 (1987).

[8] L. J. Lauhon and W. Ho, *Effects of Temperature and Other Experimental Variables on Single Molecule Vibrational Spectroscopy with the Scanning Tunneling Microscope*, Rev. Sci. Instrum. **72**, 216 (2001).

[9] J. Klein, A. Léger, M. Belin, D. Défourneau, and M. J. L. Sangster, *Inelastic-Electron-Tunneling Spectroscopy of Metal-Insulator-Metal Junctions*, Phys. Rev. B **7**, 2336 (1973).

[10] L. J. Lauhon and W. Ho, *Single-Molecule Vibrational Spectroscopy and Microscopy: CO on Cu(001) and Cu(110)*, Phys. Rev. B - Condens. Matter Mater. Phys. **60**, R8525 (1999).

[11] W. Wang, T. Lee, I. Kretzschmar, and M. A. Reed, *Inelastic Electron Tunneling Spectroscopy of an Alkanedithiol Self-Assembled Monolayer*, Nano Lett. **4**, 643 (2004).

[12] G. Czap, P. J. Wagner, F. Xue, L. Gu, J. Li, J. Yao, R. Wu, and W. Ho, *Probing and Imaging Spin Interactions with a Magnetic Single-Molecule Sensor*, Science **364**, 670 (2019).

[13] K. Nagaoka, T. Jamneala, M. Grobis, and M. F. Crommie, *Temperature Dependence of a Single Kondo Impurity*, Phys. Rev. Lett. **88**, 4 (2002).

[14] J. R. Hahn and W. Ho, *Single Molecule Imaging and Vibrational Spectroscopy with a Chemically Modified Tip of a Scanning Tunneling Microscope*, Phys. Rev. Lett. **87**, 196102 (2001).

[15] C. -l. Chiang, C. Xu, Z. Han, and W. Ho, *Real-Space Imaging of Molecular Structure and Chemical Bonding by Single-Molecule Inelastic Tunneling Probe*, Science **344**, 885 (2014).

[16] B. de la Torre, M. Švec, G. Foti, O. Krejčí, P. Hapala, A. Garcia-Lekue, T. Frederiksen, R. Zbořil, A. Arnau, H. Vázquez, and P. Jelínek, *Submolecular Resolution by Variation of the Inelastic Electron Tunneling Spectroscopy Amplitude and Its Relation to the AFM/STM Signal*, Phys. Rev. Lett. **119**, 166001 (2017).

[17] M. Ormaza, N. Bachellier, M. N. Faraggi, B. Verlhac, P. Abufager, P. Ohresser, L. Joly, M. Romeo, F. Scheurer, M.-L. Bocquet, N. Lorente, and L. Limot, *Efficient Spin-Flip Excitation of a Nickelocene Molecule*, Nano Lett. **17**, 1877 (2017).

[18] X. Chen, Construction of a Sub-Kelvin UHV Scanning Tunneling Microscope in High Magnetic Field, Cornell University, 2004.

[19] U. Ham, Construction of a Sub-Kevin Ultrahigh Vacuum Scanning Tunneling Microscope in High Magnetic Field, University of California, Irvine, 2007.

[20] C.-L. Jiang, Vibrational Inelastic Electron Tunneling Spectroscopy of Surface Adsorbed

Single Molecules at Sub-Kelvin Temperature, University of California, Irvine, 2015.

CHAPTER 2

Spin Dependent Inelastic Tunneling and Hybrid Many-body-Discrete Excitations between Two Magnetic Molecules

2.1 Abstract

Control of the spin polarization of tunneling current is paramount for the probing and manipulation of spin states at the atomic scale. Using a scanning tunneling microscope (STM), a magnetic molecule can be reproducibly transferred from the surface to the tip and forms a Kondo state. This many-body resonance undergoes exchange splitting in the proximity of another magnetic molecule adsorbed on the substrate surface and exhibits effects of spin polarization in the mutual inelastic conductance. The Kondo tip influences the inelastic spin-flip excitation in the magnetic molecule and a hybrid Kondo-spin excitation state emerges. These results reveal magnetic sensing between a many-body resonance and discrete excitations between two magnetic molecules.

2.2 Article

Spin dependent conductance has been extensively studied in a variety of systems, notably in nanoscale solid state heterojunctions, between two atoms and more recently between an atom and a molecule in the junction of a scanning tunneling microscope (STM). Spin polarization is obtained by modifying the STM tip apex with magnetic atoms like Fe or Cr [1–5]. More recently, Garnier et al. showed that the tunneling current becomes spin polarized when a cobaltocene (Bis(cyclopentadienyl)cobalt(II), $CoCp_2$) molecule attached to the STM tip apex is exposed to the exchange field of an Fe adatom [6]. The exchange interaction splits the Kondo resonance and polarizes the tunneling current in the STM junction. However, here we show that by probing a magnetic molecule, nickelocene (Bis(cyclopentadienyl)nickel(II), $NiCp_2$) adsorbed on Cu(001), the Kondo resonance of the $CoCp_2$-tip led to spin dependent inelastic spin-flip excitations of $NiCp_2$. Furthermore, a hybrid Kondo-spin excitation low energy mode was found, revealing the emergence of a man-body discrete excitation mode in a coupled system of two molecules.

The utility of the STM has been strategically enhanced through the functionalization of the STM tip with a single atom or molecule. The adsorption of xenon or carbon monoxide (CO) onto a STM tip has been shown to improve the spatial resolution of the topography images [7,8]. Additionally, CO-tip is sensitive to the local environment of the tunneling junction and can be used to probe the potential energy surface by mapping the energy shift and intensity of the hindered translation vibrational mode of CO [8–11]. While larger, more complex molecules on the tip do not improve the spatial resolution of the STM topography, $NiCp_2$-tip probes the spin exchange interactions with the sample [12–15]. More recently, $CoCp_2$-tip has been shown to exhibit a Kondo resonance, a many-body state that can be perturbed nearby spin systems [6].

As the probe molecule on the tip interacts with the sample, changes in the inelastic tunneling spectra and the emergence of hybrid modes have been observed. Spin-flip excitations [13,14], vibrational modes [11,16,17], and the combination of vibrational and spin excitations [15,18] arise from interactions between two molecules. Single-molecule Kondo systems also have satellite peaks that arise from the coupling between the zero-bias Kondo resonance and vibration modes [19–23].

The spin polarization of the tunneling current is crucial for the characterization and modification of spin systems [1,24–28]. In STM experiments, the tip can be modified to polarize the spin of the tunneling current, either by using a tip made from a magnetic metal [2], by coating a nonmagnetic metal tip with layers of magnetic material [1,3], or by picking up small clusters of magnetic atoms onto the apex of the tip [4,5]. Attaching a $CoCp_2$ molecule to the STM tip adds spin polarization in the presence of an external magnetic field. [6] The $CoCp_2$-tip also exhibits inelastic excitations and many-body physics.

In this paper, we study the interactions in the tunneling junction of a spin-1/2 $CoCp_2$-tip and a spin-1 surface-bound $NiCp_2$ on a Cu(100) surface. By the Zeeman splitting of $NiCp_2$ in an external magnetic field, we probe the effect of the $CoCp_2$-tip on the spin polarization of the tunneling conductance and the emergence of newly observable transitions from the coupling to a Kondo resonance.

Measurements were made using a home-built ultra-high vacuum STM with a base temperature of 0.5 K and a magnetic field up to 9 T normal to the sample surface. Ag tips were prepared through electrochemical etching and cycles of Ne^+ ion sputtering and annealing. The Cu(100) sample crystal was cleaned by repeated cycles of Ne^+ ion sputtering and annealing to 770 K. $CoCp_2$ and $NiCp_2$ molecules were sublimed and adsorbed onto the Cu(100) surface as

single molecules at 30 K. Both species were imaged to be tall, circular rings of different apparent heights, ~3.6 Å for $CoCp_2$ and ~2.7 Å for $NiCp_2$ (see Figure 2.6).

In the gas phase, the $CoCp_2$ molecule has an unpaired electron with a spin of ½, allowing it to act as a spin impurity. However, in the absence of an applied magnetic field and with the STM tip positioned over a $CoCp_2$ molecule adsorbed on the terrace of a Cu(100) surface, the expected Kondo resonance was not observed for the spin-1/2 impurity in the conductance (*dI/dV*) measurement. However, when the molecule is adsorbed at the step edge or transferred to the tip apex, as depicted in Fig. 2.1A, a zero bias resonance appears in the conductance spectra, as shown in Fig. 2.1B. This Kondo resonance splits in an external magnetic field (see Fig 2.1C). From the fitting of the splitting of the $CoCp_2$-tip Kondo resonance for different magnetic field strengths (see Fig. 2.1D), the effective magnetic moment is estimated to be 1.47 μ_B where μ_B is the Bohr magneton, matching bulk measurements by König et al. [29].

For a Co adatom on a Cu surface, the Kondo temperature depends on the exchange coupling and density of states of conduction electrons [30]. Assuming that the $CoCp_2$ molecule behaves similarly, the larger width of the step edge-$CoCp_2$ resonance compared to the tip-$CoCp_2$ seen in Fig. 2.1B can be explained as a consequence of greater exchange coupling to the substrate compared to the tip, increasing the Kondo temperature for the $CoCp_2$ at the step edge [31,32]. However, the Kondo resonance is absent from terrace-$CoCp_2$ despite the increased coupling with the surface conduction electrons. We explain this as an electron transfer between the molecule and terrace surface, removing the Kondo resonance by quenching the magnetic moment of the $CoCp_2$ molecule.

The Kondo resonance of $CoCp_2$ affects the $NiCp_2$ spin excitations for the $NiCp_2$/$CoCp_2$ hybrid system in Fig. 2.2. Without the $CoCp_2$ in the tunneling junction, the magnetic anisotropy

energy (MAE) is ~3.8 mV for terrace-$NiCp_2$ and ~3.95 mV for tip-$NiCp_2$, matching previously reported results. [14] For a $CoCp_2$-tip over terrace-$NiCp_2$, a split zero bias resonance and modified spin excitation peaks are observed. The low energy spin excitation peaks are slightly blue-shifted from ~2.6 to ~2.8 meV and broadened while the high energy peaks are attenuated and each peak has an asymmetric line shape. For a $NiCp_2$ tip over a step edge $CoCp_2$, the zero bias excitation is absent, the spin excitation peaks are not blue-shifted, and the higher energy spin excitation peak is attenuated.

For $NiCp_2$, each peak can be characterized by the spin of the electron involved in the spin excitation in the tunneling junction. For example, the $m_s = 0$ to $m_s = 1$ transition at positive bias requires the electron tunneling from the tip to the molecule to have a spin of +1/2 in order to conserve the total angular momentum. At the same time, the spin excitation for the same transition at negative bias would require an electron with a spin of -1/2 tunneling from the molecule to the tip. Consequentially, we can measure the effect of the junction on the tunneling current spin by comparing the ratio of the intensities of the peaks at positive and negative biases for the same excitation.

The spin asymmetry of the tunneling current is calculated as $\eta = (h_+ - h_-)/(h_+ + h_-)$, where h_+ (h_-) is the height of a peak with s = +1/2 (-1/2) for the tunneling electrons. For the bare tip on terrace-$NiCp_2$ and the $NiCp_2$-tip over the bare substrate, η is only 0.03 from IETS spectra shown in Fig. 2.2, indicating that a $NiCp_2$ does not have inherent spin asymmetry in the presence of an external magnetic field. With the $NiCp_2$-tip positioned over a step edge-$CoCp_2$, the spin asymmetry increases to ~0.21, favoring the electron magnetic moment aligning with the external magnetic field. The spin asymmetry becomes ~0.10 when the $CoCp_2$-tip is positioned over a

terrace-$NiCp_2$. The measured asymmetry for this $CoCp_2$-tip agrees with the simulation data calculated by Leo Garnier et al. [6].

While the MAE and Zeeman splitting of $NiCp_2$ alone agree with previously reported results, we find that the dependence of the peak position on the magnetic field strength also points to an additional peak from the Kondo resonance. In Fig. 2.3A, we see that the MAE of the tip-$NiCp_2$ is unaffected by the magnetic field, but when positioned over the step edge-$CoCp_2$, the low energy spin flip peak is blue shifted while the high energy peak is unchanged. This suggests the addition of hybrid $CoCp_2$ Kondo and $NiCp_2$ spin excitation modes as the shift in energy is roughly half of the Zeeman splitting of the $CoCp_2$ Kondo resonance shown in Fig. 2.1D. In Fig. 2.3C, the $CoCp_2$-tip over terrace-$NiCp_2$ shows a peak splitting of the low energy spin excitation. The peaks at ~2.7 meV and ~4.3 meV match the $NiCp_2$ alone low and high energy spin excitations at -9 Tesla. The energy of the new peak at ~3.4 meV equals the sum of the unperturbed low energy $NiCp_2$ spin excitation and the Zeeman split $CoCp_2$ Kondo resonance. We assign this ~3.4 meV peak as a hybrid $CoCp_2$ Kondo $NiCp_2$ spin excitation.

The introduction of hybrid $CoCp_2$ Kondo and $NiCp_2$ spin excitation modes, as shown in Fig. 2.3C, can explain the changes to the excitations seen in the $NiCp_2/CoCp_2$ hybrid system. First, the line shape of the spin excitations changes from Gaussian to the asymmetric Fano-Frota line shape characteristic of a Kondo resonance peak. Second, the peak width of the low energy spin excitation peak increases, which implies either a change in the intrinsic width of the spin excitation or a second peak of similar energy is overlapping with the original spin excitation peak. Third, the intensity of the low energy peak increases significantly without a change in the tip-sample distance while the high energy peak intensity remains unchanged.

The $CoCp_2$-$NiCp_2$ system can be described with a simplified model Hamiltonian:

$$\widehat{H}_s = D_1(\hat{S}_{1z}^2) - g_1\mu B_{ext}(\hat{S}_{1z}) - g_2\mu B_{ext}(\hat{S}_{2z})$$

The first term represents the uniaxial magnetic anisotropy energy of the $NiCp_2$ molecule and the last two terms are the Zeeman energy of the spin of each molecule in an external magnetic field. Here we ignore any dipole-dipole or spin exchange interactions for the simplicity of the model. Using this Hamiltonian and modeling the $NiCp_2$ as a spin-1 system and $CoCp_2$ as a spin-1/2 system, we get one ground state and five excited states with an applied magnetic field. The MAE of $NiCp_2$ and the g value of $CoCp_2$ are in excellent agreement with the experimentally measured peaks, showing the five excited state transitions, with one exception. The high energy hybrid $CoCp_2$ Kondo and $NiCp_2$ spin excitation is not observed as it is a $\Delta m_s = -2$ transition and thus forbidden by spin angular momentum conservation for a single tunneling electron.

The sensitivity of the hybrid mode to the geometry in the tunneling junction motivated a study of the lateral spatial dependence, shown in Fig. 2.4. IETS spectra were taken with the tunneling gap set to 18mV/100pA and advanced 0.56 Å after turning of the feedback. The low energy $NiCp_2$ spin excitation at ~2.7 meV is unaffected by the lateral position of the $CoCp_2$-tip, but the hybrid mode around ~3.4 meV shifts noticeably. We also find that the apparent intensity of the high energy spin excitation at ~4.4 meV is attenuated by both the spin asymmetry of the $CoCp_2$ tip and the Fano line shape of the hybrid mode.

As the low energy spin excitation peak does not shift as the $CoCp_2$-tip positions over the $NiCp_2$, the energy shift of the hybrid mode arises from either a shift in the Kondo feature or the coupling between the Kondo and spin excitations. The Kondo spin excitation energy is determined by the magnetic moment of the $CoCp_2$ and the external magnetic field strength. However, the hybrid excitation has a Fano line shape, not a Gaussian line shape. The position of the peak maximum for a Fano-Frota peak is also shifted by the asymmetry ratio (see Fig. 2.5).

The asymmetry ratio has been shown to change due to the interference of tunneling channels [33,34]. As the hybrid mode shares the Fano line shape with the split Kondo peak, the energy shift is due primarily to the changes in the tunneling channel interference as the tip positions laterally.

In summary, we have shown that the spin asymmetry of the tunneling junction is modified by the attachment of a $CoCp_2$ molecule to the tip and the coupling between the adsorbed molecule, surface, and $CoCp_2$-tip. The $NiCp_2$-$CoCp_2$ system shows a hybrid mode of Kondo resonance and spin excitation. The hybrid mode peak shares the Fano line shape and asymmetry shift over the $NiCp_2$ molecule that is expected of a Kondo resonance. Further investigation into other possible hybrid modes between $CoCp_2$ and other systems may reveal inelastic transitions too weak to be observed by conventional STM-IETS.

Support of this research by the Office of Naval Research under Grant No. N00014-20-1-2475 is gratefully acknowledged.

2.3 Supplementary Materials

2.3.1 Transfer Procedures for $NiCp_2$ and $CoCp_2$

To pick up a $NiCp_2$ molecule from the terrace to the STM tip, we first position the tip over the center of the ring. The feedback setpoint is set to 70mV/40pA before opening the circuit. With the feedback circuit open, we advance the tip to the molecule slowly until there is a sudden change in the tunneling current without a change in the position of the tip, marking the molecule adsorbing to the tip apex. The molecule usually moves to the tip when it is advanced 7-8 Å in from the initial setpoint. With the $NiCp_2$ on the tip, we step the tip back away from the surface until the feedback circuit can be restored. To pick up a $CoCp_2$ molecule, we find that

positioning the tip over the center of the molecule is not the best position. Instead, we perform a topography scan over the molecule at a closer feedback setpoint. Typically, 10mV/500pA is close enough for the molecule to move to the tip, which is marked by a sudden change in the feedback output voltage. Once the change has occurred, we interrupt the topography scan and change the feedback setpoint to a more stable setting.

To drop the $NiCp_2$ or $CoCp_2$ molecule from the tip apex nondestructively, we position the tip over a clean space on the terrace before opening the feedback circuit. We then slowly ramp the bias to ~1.5V or until there is a sharp change in the tunneling current. If the bias reaches 1.5V before the molecule has dropped from the tip, we restore the bias to the setpoint before the feedback loop was opened and bring the tip closer to the surface before trying again. This method does not always drop the molecule, but it does not risk changing the tip apex. If this procedure does not work, we have found that lightly "poking" the tip into the surface, bringing it just into contact with the surface multiple times is more likely to drop the molecule, but also risks dulling the tip.

2.3.2 Fano Frota Line Shape Fitting

The fitting used for the Kondo resonance in conductance (*dI/dV*) spectra is given by the Fano-Frota line shape, given by

$$\frac{\partial I}{\partial V}(r,V) = A\,(r)\,\frac{(q+\epsilon)^2}{1+\epsilon^2} + c,$$

where

$$\epsilon = \frac{eV - E_0}{\Gamma}.$$

Here, E_0 is the resonance energy of the fitted peak, q is the asymmetry parameter, and Γ is the peak broadening term tied to the Kondo temperature of the system in question. The expression used for Kondo resonance in IETS (d^2I/dV^2) spectra is given by

$$\frac{\partial^2 I}{\partial V^2}(r,V) = \frac{2}{\Gamma}A(r)\frac{(q+\epsilon)(1-q\epsilon)}{(1+\epsilon^2)^2} + c.$$

In Fig. 2.5, plots of this peak fit are given for varying q asymmetry values to show that the resonance energy of the peak is not given by the center of the local maximum of the fitted peak. In the case of a spin-1/2 impurity in the tunneling junction, the asymmetry parameter is controlled by the interference between the tunneling channels through the impurity and directly to the conducting surface [33,34].

2.3.3 Additional Figure Discussion

The topography image of a $CoCp_2$ adsorbed on the Cu(001) surface reveals some information about the presence of the Kondo resonance, but the details require further investigation. In Fig. 2.6, representative terrace-$NiCp_2$ and terrace-$CoCp_2$ are shown to be rings when imaged with either a bare tip or $CoCp_2$ tip. Every terrace-$CoCp_2$ studied had no Kondo resonance in the conductance spectra. Similarly, every step-edge $CoCp_2$ was imaged as a crescent shape on the step edge of the Cu(001) surface and had a Kondo resonance. However, the Kondo temperature for each molecule varied due to the differences in coupling from different step edge directions and step edge-$CoCp_2$ adsorption sites.

The width, amplitude and asymmetry of the Kondo resonance also depends on the distances between tip, $CoCp_2$ and Cu(001) surface. In Fig. 2.7, bringing the tip-$CoCp_2$ closer to the surface increases the width of the Kondo resonance peak. The width of a peak detected by

STM-IETS is determined by the sample temperature, the lock-in detection modulation bias amplitude, and the intrinsic width of the peak itself expressed as

$$W = \sqrt{W_I^2 + (1.7\, V_{mod})^2 + (5.4\, k_B T/e)^2}.$$

With the temperature and modulation bias amplitude held constant, the broadening of the Kondo peak is due to the increase of the Kondo temperature because of increased coupling with the surface conduction electrons.

By reducing the coupling with the surface, we also see the Kondo resonance disappear in Fig 2.8. Moving the tip-$CoCp_2$ away from the surface not only decreases surface coupling, but also decreases the total tunneling current, making detection of any IETS feature impossible. Positioning the tip-$CoCp_2$ over a surface-$CoCp_2$ maintains the tunneling current without including surface coupling thanks to the height of the surface-$CoCp_2$. In this configuration, the Kondo resonance is suppressed, either from the lack of surface coupling or some interference from the surface-$CoCp_2$. The Kondo resonance is absent in both the tip-$CoCp_2$ over surface-$CoCp_2$ system and the bare tip over surface-$CoCp_2$ system.

In Fig. 2.9, we expand on the study of lateral spatial dependence over the step edge-$CoCp_2$. By extending the range of the IETS spectra, we observe a Fano line shape peak at ~50 meV that we assign to be a Kondo satellite peak. Kondo satellite peaks are the consequence of coupling between the Kondo resonance and an electron-vibration interaction of a Kondo system [21–23]. As the tip is positioned laterally over the step edge-$CoCp_2$, both the Kondo resonance and the Kondo satellite peaks shift in intensity relative to each other. The intensity of the satellite peak reaches a maximum between the lobes seen in the topography in Fig. 2.9B while the Kondo resonance is stronger on the lobes. Varying the tip height does not cause similar shifts to the Kondo resonance and satellite peaks. Fig. 2.10 shows the evolution of the topography over step edge-$CoCp_2$ as the sample bias steps through the energy of the satellite

peak. The change from the two lobe shape to the crescent shape supports the fact that the maximum of the satellite peak intensity is localized between the lobes.

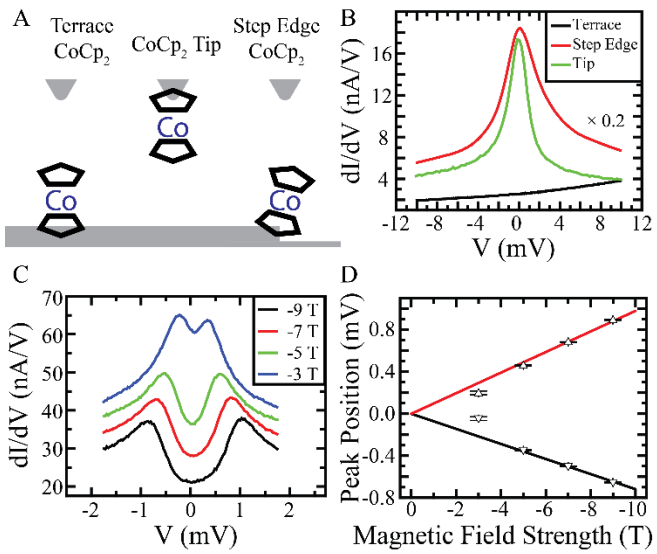

Figure 2.1: Properties of $CoCp_2$ on Cu(001) surface and attached to STM tip.

(A) Schematic of three different $CoCp_2$ adsorption geometries. (B) Conductance (*dI/dV*) spectra of each adsorption geometry. Spectra were taken at a feedback setpoint of 100mV/100pA with the feedback turned off, advanced 2.2 Å toward the surface (70mV/40pA, 2.8 Å advance for spectroscopy of molecule adsorbed on terrace). (C) Conductance spectra of $CoCp_2$ attached to the tip ($CoCp_2$-tip) at different magnetic field strengths. Spectra were taken at a feedback set point of 18mV/100pA. Each plot is offset for clarity. (D) Zeeman splitting of zero bias resonance of $CoCp_2$-tip as a function of the applied magnetic field.

Figure 2.2: STM-IETS of $NiCp_2$ and $CoCp_2$ Hybrid System.

STM-IETS measurements taken at B_{ext} = -9 T, acquired at a feedback setpoint of 18mV/100pA and advanced 1.1 Å toward the surface. The nomenclatures denote the locations of the two molecules, for example $CoCp_2/NiCp_2$ denotes $CoCp_2$ attached to the tip ($CoCp_2$-tip) probing $NiCp_2$ adsorbed on the Cu(001) surface; Bare denotes the bare tip, Bkg denotes the Cu(001) substrate surface. Spectra are offset for clarity.

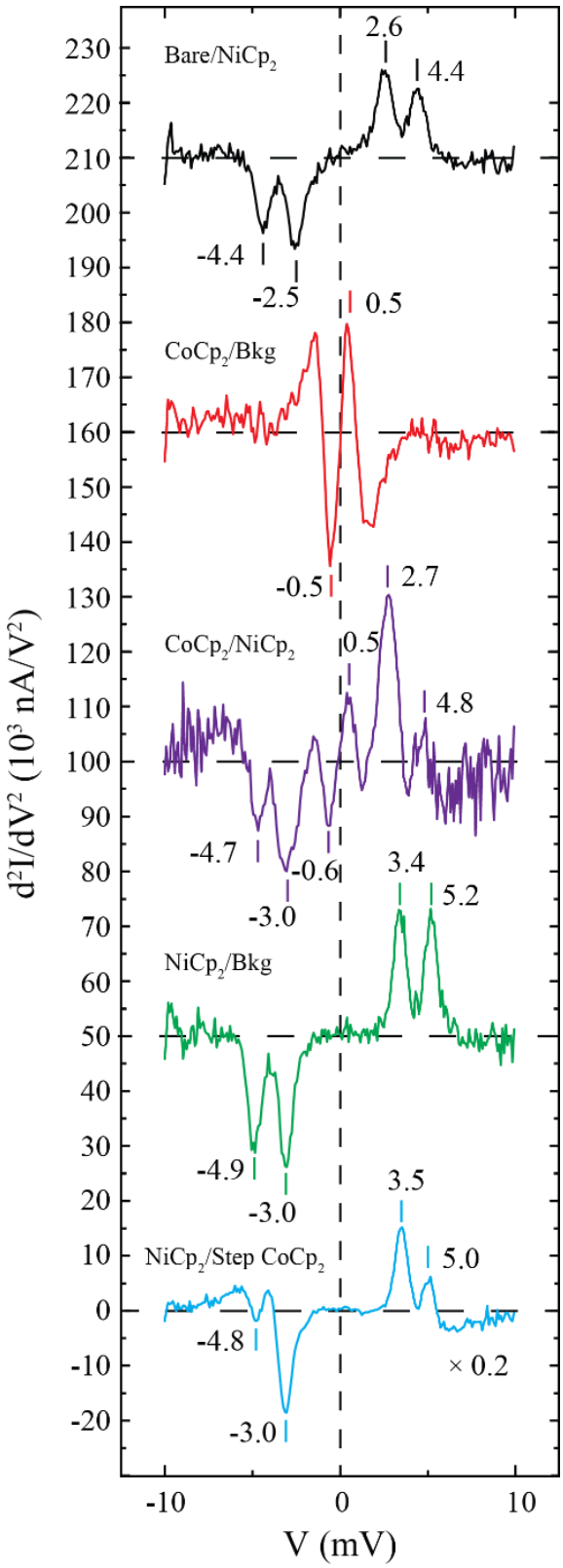
Bare/NiCp2
2.6
4.4
-4.4
-2.5
0.5
CoCp2/Bkg
-0.5
2.7
CoCp2/NiCp2
0.5
4.8
-4.7
-0.6
-3.0
3.4
5.2
NiCp2/Bkg
-4.9
-3.0
3.5
NiCp2/Step CoCp2
5.0
-4.8
× 0.2
-3.0
d2I/dV2 (103 nA/V2)
V (mV)

Figure 2.3: Probing Hybrid $CoCp_2$ Kondo and $NiCp_2$ Spin Excitation Modes.

(A) Magnetic field dependence (0 to -9 Tesla, with field pointing into the substrate surface) of IETS spectroscopy for $NiCp_2$-tip probing $CoCp_2$ adsorbed at step edge of Cu(001) (dark spectra) compared to $NiCp_2$-tip over Cu(001) background (light spectra). Tip height was determined with set point at 18mV/100pA (18mV/300pA for 0 T curve) then advancing the tip 1.1 Å toward the surface. (B) Energy level diagram for $NiCp_2$ tip on $CoCp_2$ adsorbed on terrace of Cu(001) surface (terrace-$CoCp_2$), showing $NiCp_2$ magnetic anisotropy energy D, $NiCp_2$ Zeeman splitting E_{z1}, and $CoCp_2$ Zeeman splitting E_{z2} applied to each pair of states. The horizontal dashed line denote the Fermi level at zero bias. (C) IETS spectroscopy for $CoCp_2$-tip over $NiCp_2$ adsorbed on the Cu(001) terrace with B_{ext}= -9 T. Tip height was determined by opening the feedback set point at 18mV/100pA then advancing 0.56 Å toward the surface. The spectra were acquired with 100 μV bias steps in (A) or 30 μV in (C). The insert depicts the geometry for the coupling between the two molecules.

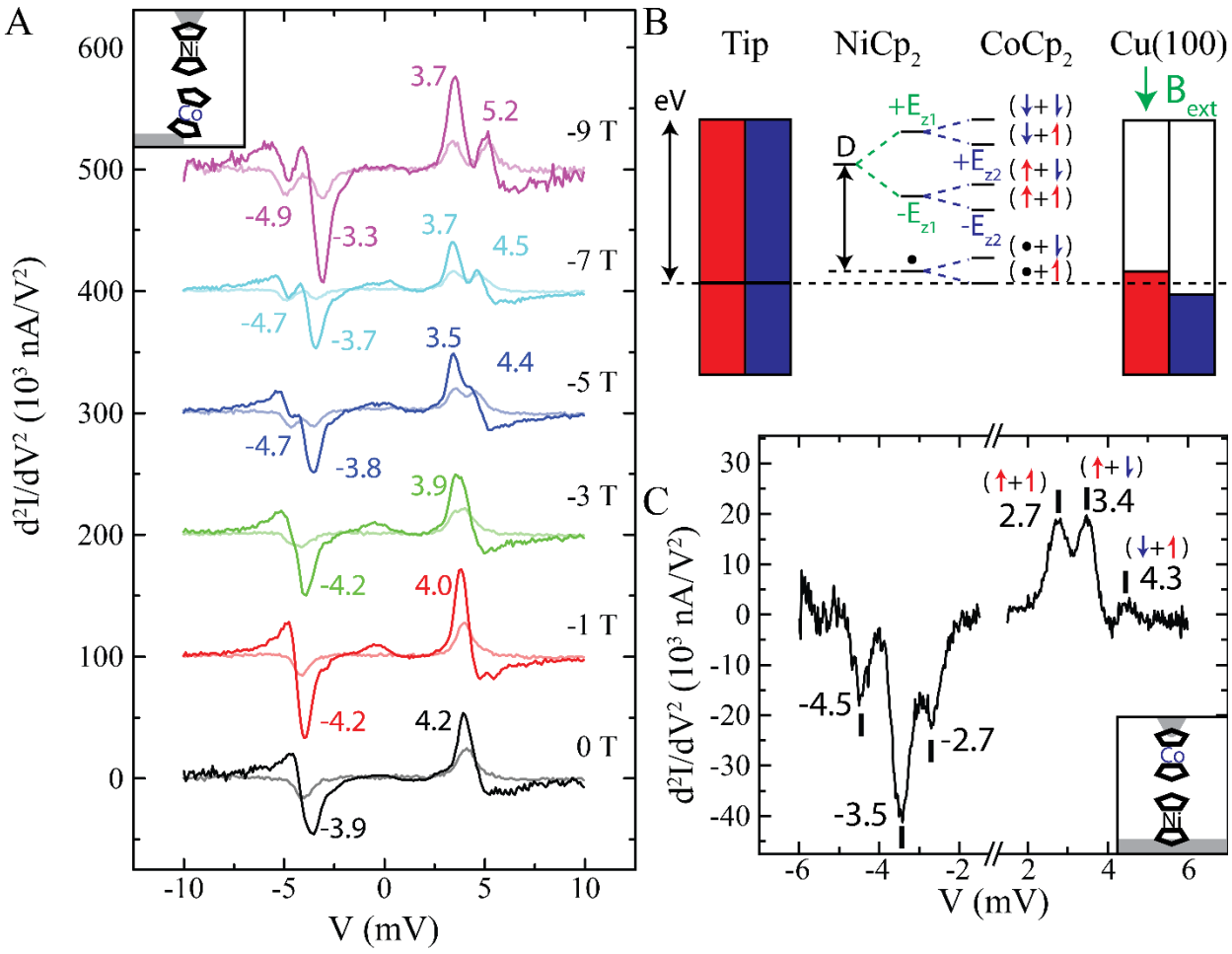
A
B
C
Tip
NiCp2
CoCp2
Cu(100)
eV
D
+Ez1
-Ez1
+Ez2
-Ez2
Bext
(↓+↓)
(↓+↑)
(↑+↓)
(↑+↑)
(•+↓)
(•+↑)
-9 T
-7 T
-5 T
-3 T
-1 T
0 T
3.7
5.2
-4.9
-3.3
3.7
4.5
-4.7
-3.7
3.5
4.4
-4.7
-3.8
3.9
-4.2
4.0
-4.2
4.2
-3.9
d²I/dV² (10³ nA/V²)
V (mV)
2.7
3.4
4.3
-4.5
-2.7
-3.5
Ni
Co

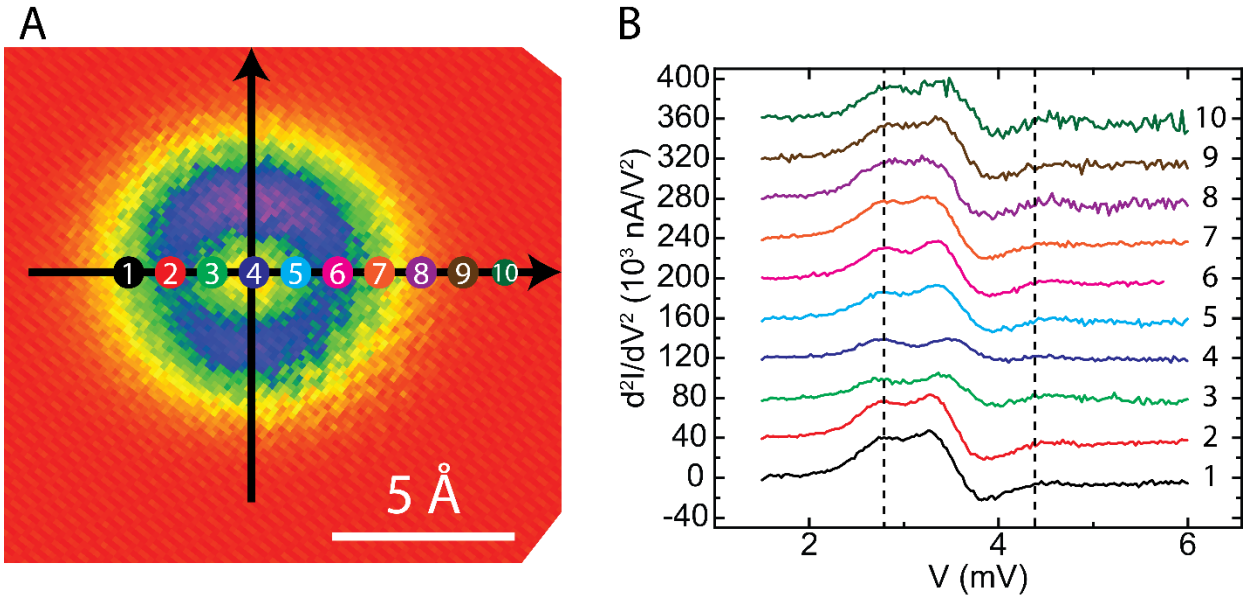

Figure 2.4: Lateral Dependence of Hybrid $CoCp_2$ Kondo and $NiCp_2$ Spin Excitation Modes (A) Topography taken with $CoCp_2$-tip over terrace-$NiCp_2$ with B_{ext} = -9 T. (B) IETS spectroscopy taken at different lateral positions over the terrace-$NiCp_2$, as indicated by the dots in A and labelled by positions 1 to 10. Tip height was determined by opening the feedback at set point of 18mV/100pA then advancing 0.56 Å toward the surface. Three peaks can be identified at ~2.7meV, ~3.3 meV, and ~4.5 meV. The highest energy peak at ~4.5 meV is strongly attenuated by the spin polarization of $CoCp_2$-tip.

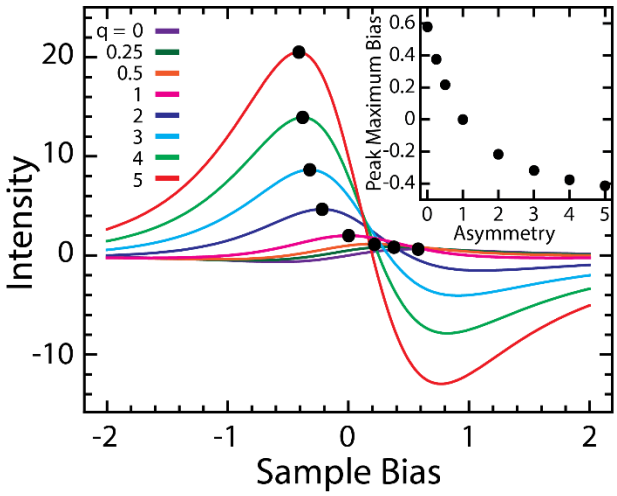

Figure 2.5: Comparison of Fitted Fano Line Shapes for Different Asymmetry Values. Peak maxima are marked by black dots. Fixed parameters for each plot are $A = 1$, $E_0 = 0$, and $\Gamma = 1$. Inset shows the bias of the peak maximum value as a function of the asymmetry parameter.

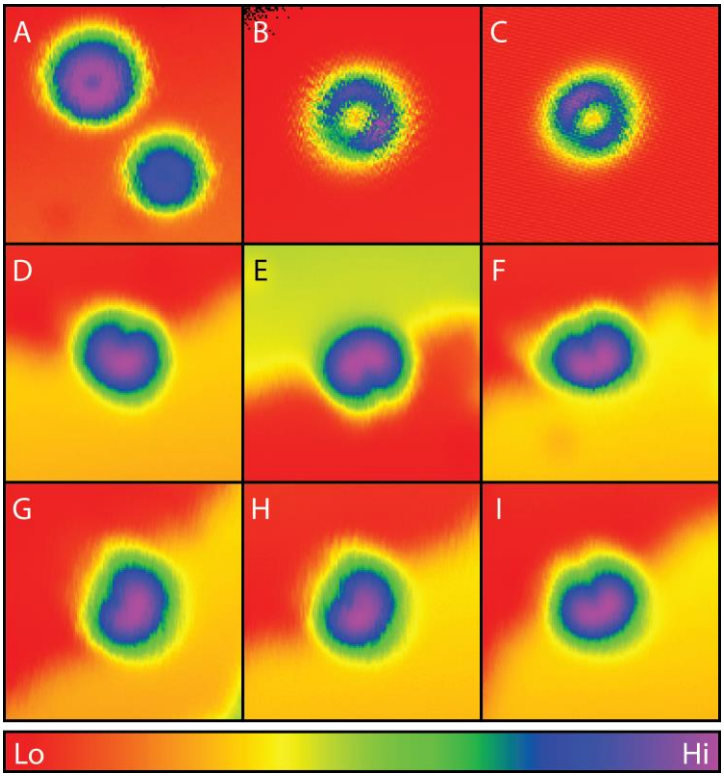

Figure 2.6: Topography of $CoCp_2$ and $NiCp_2$ on Cu(001) Terrace and Step Edge. (A) Topography of $CoCp_2$ (top left) and $NiCp_2$ (bottom right) molecules taken with bare tip at a feedback set point of 70mV/40pA. Image is 4 nm by 4 nm. (B-C) Constant height images of $CoCp_2$ (B) and $NiCp_2$ (C) taken with $CoCp_2$ tip. Each image is 2 nm by 2 nm. (D-I) Topography images of different step edge $CoCp_2$ molecules taken at a feedback set point of 100mV/100pA. Each image is 4 nm by 4 nm.

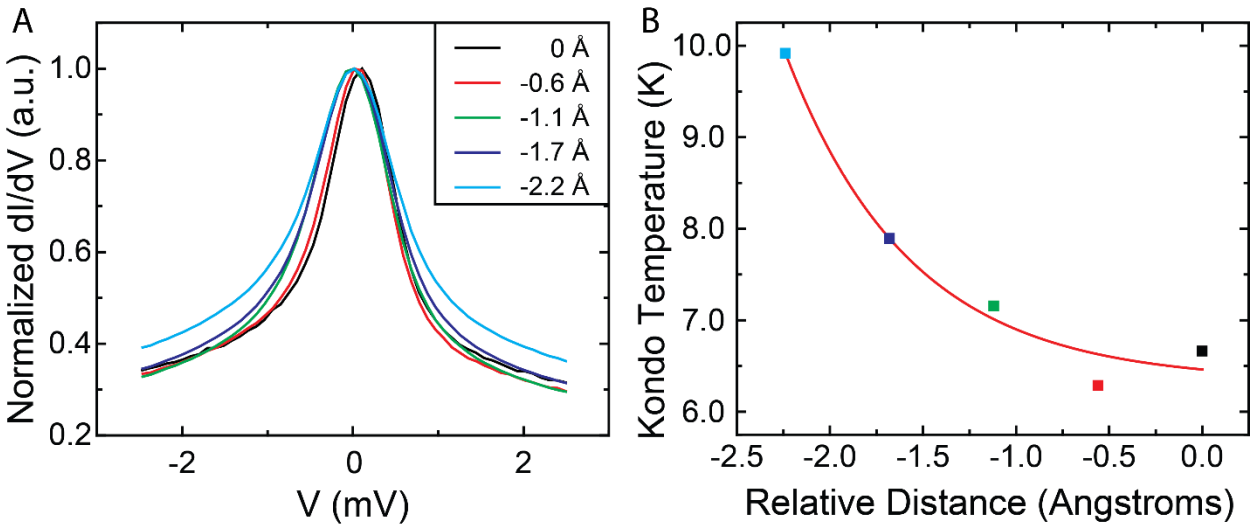

Figure 2.7: Tip Height Dependence of Tip-$CoCp_2$ Kondo Temperature.

(A) STM-IETS measurements of tip-CoCp2 over Cu(001) terrace at varying tip heights. Initial tip height is defined by opening the feedback loop at 175mV/100pA and advancing 2.2 Å towards the surface. (B) Plot of Kondo temperature of tip-$CoCp_2$ calculated from peak width, STM temperature, and lock-in modulation bias.

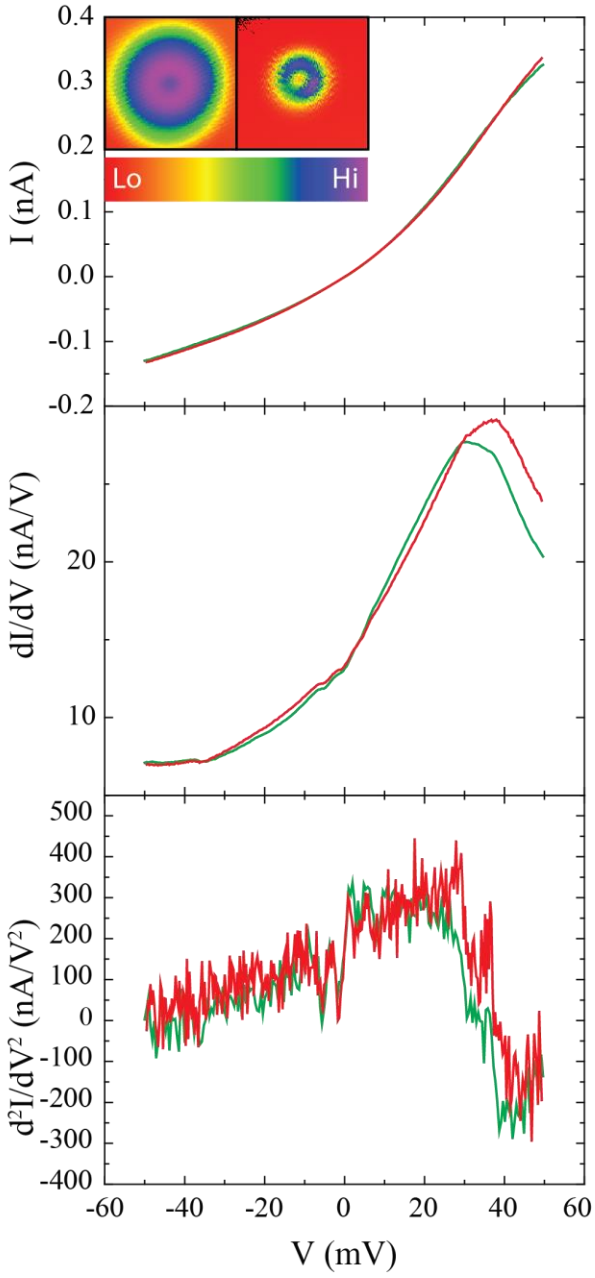

Figure 2.8: Comparison of Bare Tip and Tip-$CoCp_2$ IETS on Terrace-$CoCp_2$.

I-V, conductance (dI/dV) and IETS (d^2I/dV^2) spectra of bare Ag tip (red) and $CoCp_2$ tip (green) on $CoCp_2$ adsorbed on Cu(001) terrace taken with an external B field of -1 T. Inset shows topography of terrace-$CoCp_2$ taken with bare tip and constant height image taken with $CoCp_2$ attached to tip. The tip was positioned over the center of the molecule with a feedback set point of 70mV/40pA before opening the feedback circuit and advancing 2.2 Å.

Figure 2.9: Lateral Dependence IETS Measurements of Bare Tip on Step Edge-$CoCp_2$. (A) STM topography of step edge-$CoCp_2$ taken at a feedback set point of 100mV/100pA. STM topography and IETS measurements of step edge-$CoCp_2$ taken along the step edge (B,D) and across the step edge (C,E). Topography feedback set point is 18mV/100pA and IETS setpoint is 100mV/100pA, advanced 2.2 Å to surface. Inset in D and E focus on negative bias inelastic peaks for more detail. (F) IETS spectra tip height series with the tip positioned over the center of the molecule and initial height set by feedback set point of 100mV/100pA.

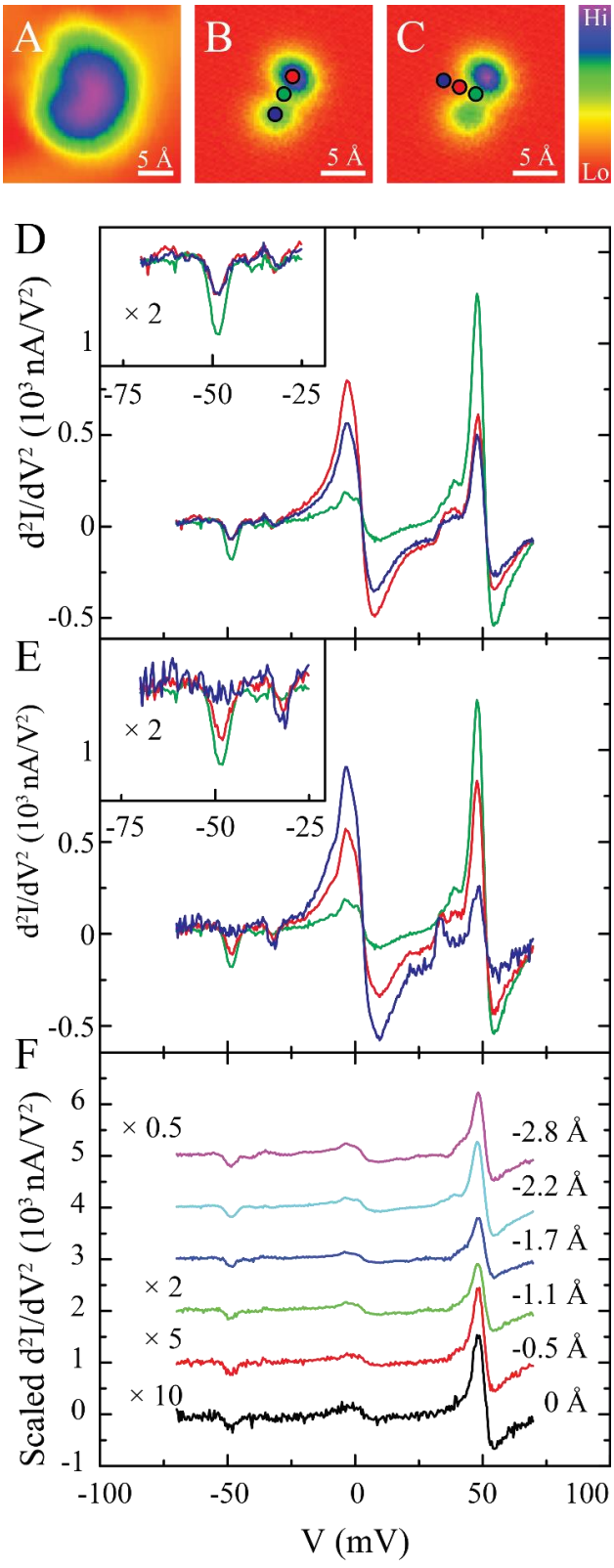
A
B
C
5 Å
5 Å
5 Å
Hi
Lo
D
E
F
× 2
× 2
× 0.5
× 2
× 5
× 10
-2.8 Å
-2.2 Å
-1.7 Å
-1.1 Å
-0.5 Å
0 Å
d²I/dV² (10³ nA/V²)
Scaled d²I/dV² (10³ nA/V²)
V (mV)

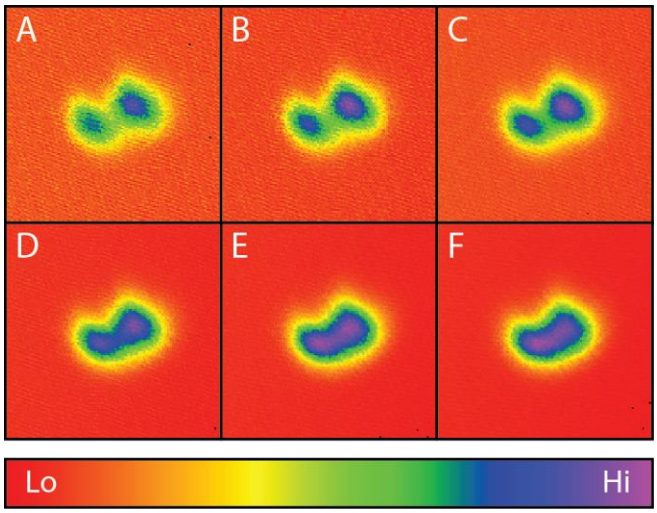

Figure 2.10: Constant Height STM Topography of Step Edge-CoCp2 Acquired at Different Sample Biases.

Images taken with a bare tip with the feedback circuit opened with the tip positioned over the center of the molecule with a set point of 100mV/100pA. After the feedback circuit is opened, the tip-sample bias is changed to (A) 18mV, (B) 25mV, (C) 40mV, (D) 60mV, (E) 80mV, (F) 100mV before scanning. Each image is 2 nm by 2 nm.

Table 2.1: Spin Asymmetry Values for B = -9 T from Fig. 2

Geometry	Low Energy η	High Energy η	Average η
Bare/$NiCp_2$	-0.036 ± 0.013	-0.013 ± 0.039	-0.025 ± 0.024
$NiCp_2$/Background	0.064 ± 0.027	0.011 ± 0.030	0.037 ± 0.020
$CoCp_2$/$NiCp_2$	0.022 ± 0.037	0.182 ± 0.092	0.102 ± 0.050
$NiCp_2$/Step Edge $CoCp_2$	0.039 ± 0.016	0.385 ± 0.051	0.213 ± 0.027

Table 2.2: Spin Asymmetry Values for $NiCp_2$/Step Edge $CoCp_2$ from Fig. 3

Magnetic Field	Low Energy η	High Energy η	Average η
-5 T	0.053 ± 0.124	0.223 ± 0.215	0.138 ± 0.124
-7 T	0.096 ± 0.043	0.613 ± 0.235	0.354 ± 0.120
-9 T	0.039 ± 0.016	0.385 ± 0.051	0.213 ± 0.027

References and Notes

[1] A. Kubetzka, M. Bode, O. Pietzsch, and R. Wiesendanger, *Spin-Polarized Scanning Tunneling Microscopy with Antiferromagnetic Probe Tips*, Phys. Rev. Lett. **88**, 057201 (2002).

[2] L. Schneider, P. Beck, J. Wiebe, and R. Wiesendanger, *Atomic-Scale Spin-Polarization Maps Using Functionalized Superconducting Probes*, Sci. Adv. **7**, eabd7302 (2021).

[3] E. Sierda, M. Elsebach, R. Wiesendanger, and M. Bazarnik, *Probing Weakly Hybridized Magnetic Molecules by Single-Atom Magnetometry*, Nano Lett. **19**, 9013 (2019).

[4] L. Malavolti, G. McMurtrie, S. Rolf-Pissarczyk, S. Yan, J. A. J. Burgess, and S. Loth, *Minimally Invasive Spin Sensing with Scanning Tunneling Microscopy*, Nanoscale **12**, 11619 (2020).

[5] S. Loth, K. von Bergmann, M. Ternes, A. F. Otte, C. P. Lutz, and A. J. Heinrich, *Controlling the State of Quantum Spins with Electric Currents*, Nat. Phys. **6**, 340 (2010).

[6] L. Garnier, B. Verlhac, P. Abufager, N. Lorente, M. Ormaza, and L. Limot, *The Kondo Effect of a Molecular Tip As a Magnetic Sensor*, Nano Lett. **20**, 8193 (2020).

[7] G. Kichin, C. Wagner, F. S. Tautz, and R. Temirov, *Calibrating Atomic-Scale Force Sensors Installed at the Tip Apex of a Scanning Tunneling Microscope*, Phys. Rev. B **87**, 081408 (2013).

[8] P. Hapala, G. Kichin, C. Wagner, F. S. Tautz, R. Temirov, and P. Jelínek, *Mechanism of High-Resolution STM/AFM Imaging with Functionalized Tips*, Phys. Rev. B **90**, 085421 (2014).

[9] A. Garcia-Lekue, D. Sanchez-Portal, A. Arnau, and T. Frederiksen, *Simulation of Inelastic Electron Tunneling Spectroscopy of Single Molecules with Functionalized Tips*, Phys.

Rev. B **83**, 155417 (2011).

[10] P. Hapala, R. Temirov, F. S. Tautz, and P. Jelínek, *Origin of High-Resolution IETS-STM Images of Organic Molecules with Functionalized Tips*, Phys. Rev. Lett. **113**, 226101 (2014).

[11] Z. Han, G. Czap, C. Xu, C. Chiang, D. Yuan, R. Wu, and W. Ho, *Probing Intermolecular Coupled Vibrations between Two Molecules*, Phys. Rev. Lett. **118**, 036801 (2017).

[12] B. Verlhac, N. Bachellier, L. Garnier, M. Ormaza, P. Abufager, R. Robles, M.-L. Bocquet, M. Ternes, N. Lorente, and L. Limot, *Atomic-Scale Spin Sensing with a Single Molecule at the Apex of a Scanning Tunneling Microscope*, Science **366**, 623 (2019).

[13] M. Ormaza, N. Bachellier, M. N. Faraggi, B. Verlhac, P. Abufager, P. Ohresser, L. Joly, M. Romeo, F. Scheurer, M.-L. Bocquet, N. Lorente, and L. Limot, *Efficient Spin-Flip Excitation of a Nickelocene Molecule*, Nano Lett. **17**, 1877 (2017).

[14] G. Czap, P. J. Wagner, F. Xue, L. Gu, J. Li, J. Yao, R. Wu, and W. Ho, *Probing and Imaging Spin Interactions with a Magnetic Single-Molecule Sensor*, Science **364**, 670 (2019).

[15] G. Czap, P. J. Wagner, J. Li, F. Xue, J. Yao, R. Wu, and W. Ho, *Detection of Spin-Vibration States in Single Magnetic Molecules*, Phys. Rev. Lett. **123**, 106803 (2019).

[16] K.-A. Wang, A. M. Rao, P. C. Eklund, M. S. Dresselhaus, and G. Dresselhaus, *Observation of Higher-Order Infrared Modes in Solid C60 Films*, Phys. Rev. B **48**, 11375 (1993).

[17] Z.-H. Dong, P. Zhou, J. M. Holden, P. C. Eklund, M. S. Dresselhaus, and G. Dresselhaus, *Observation of Higher-Order Raman Modes in C60 Films*, Phys. Rev. B **48**, 2862 (1993).

[18] N. Bachellier, B. Verlhac, L. Garnier, J. Zaldívar, C. Rubio-Verdú, P. Abufager, M.

Ormaza, D.-J. Choi, M.-L. Bocquet, J. I. Pascual, N. Lorente, and L. Limot, *Vibron-Assisted Spin Excitation in a Magnetically Anisotropic Molecule*, Nat. Commun. **11**, 1619 (2020).

[19] L. H. Yu, Z. K. Keane, J. W. Ciszek, L. Cheng, M. P. Stewart, J. M. Tour, and D. Natelson, *Inelastic Electron Tunneling via Molecular Vibrations in Single-Molecule Transistors*, Phys. Rev. Lett. **93**, 266802 (2004).

[20] I. Fernández-Torrente, K. J. Franke, and J. I. Pascual, *Vibrational Kondo Effect in Pure Organic Charge-Transfer Assemblies*, Phys. Rev. Lett. **101**, 217203 (2008).

[21] D. Rakhmilevitch, R. Korytár, A. Bagrets, F. Evers, and O. Tal, *Electron-Vibration Interaction in the Presence of a Switchable Kondo Resonance Realized in a Molecular Junction*, Phys. Rev. Lett. **113**, 236603 (2014).

[22] P. Roura-Bas, L. Tosi, and A. A. Aligia, *Replicas of the Kondo Peak Due to Electron-Vibration Interaction in Molecular Transport Properties*, Phys. Rev. B **93**, 115139 (2016).

[23] J. J. Parks, A. R. Champagne, G. R. Hutchison, S. Flores-Torres, H. D. Abruña, and D. C. Ralph, *Tuning the Kondo Effect with a Mechanically Controllable Break Junction*, Phys. Rev. Lett. **99**, 026601 (2007).

[24] K. von Bergmann, M. Ternes, S. Loth, C. P. Lutz, and A. J. Heinrich, *Spin Polarization of the Split Kondo State*, Phys. Rev. Lett. **114**, 076601 (2015).

[25] X.-X. Fu, F. Wei, Y. Niu, and C.-K. Wang, *Designing High-Performance Spin Filters and Valves Based on Metal-Salophen Molecular Chains*, Phys. E Low-Dimensional Syst. Nanostructures **131**, 114737 (2021).

[26] L. Bogani and W. Wernsdorfer, *Molecular Spintronics Using Single-Molecule Magnets*, Nat. Mater. **7**, 179 (2008).

[27] S. Krause, L. Berbil-Bautista, G. Herzog, M. Bode, and R. Wiesendanger, *Current-Induced Magnetization Switching with a Spin-Polarized Scanning Tunneling Microscope*, Science **317**, 1537 (2007).

[28] A. A. Khajetoorians, B. Baxevanis, C. Hübner, T. Schlenk, S. Krause, T. O. Wehling, S. Lounis, A. Lichtenstein, D. Pfannkuche, J. Wiebe, and R. Wiesendanger, *Current-Driven Spin Dynamics of Artificially Constructed Quantum Magnets*, Science **339**, 55 (2013).

[29] E. König, R. Schnakig, S. Kremer, B. Kanellakopulos, and R. Klenze, *Magnetism between 0.90 and 300 K and Complete Ligand Field Theory for Chromocene and Cobaltocene*, Chem. Phys. **27**, 331 (1978).

[30] N. Knorr, M. A. Schneider, L. Diekhöner, P. Wahl, and K. Kern, *Kondo Effect of Single Co Adatoms on Cu Surfaces*, Phys. Rev. Lett. **88**, 4 (2002).

[31] K. Iwata, T. Miyamachi, E. Minamitani, and F. Komori, *Sensing Surface Lattice Strain with Kondo Resonance of Single Co Adatom*, Appl. Phys. Lett. **116**, 051604 (2020).

[32] R. Hiraoka, E. Minamitani, R. Arafune, N. Tsukahara, S. Watanabe, M. Kawai, and N. Takagi, *Single-Molecule Quantum Dot as a Kondo Simulator*, Nat. Commun. **8**, 16012 (2017).

[33] L. Farinacci, G. Ahmadi, M. Ruby, G. Reecht, B. W. Heinrich, C. Czekelius, F. von Oppen, and K. J. Franke, *Interfering Tunneling Paths through Magnetic Molecules on Superconductors: Asymmetries of Kondo and Yu-Shiba-Rusinov Resonances*, Phys. Rev. Lett. **125**, 256805 (2020).

[34] D. Jacob, *Simulation of Inelastic Spin Flip Excitations and Kondo Effect in STM Spectroscopy of Magnetic Molecules on Metal Substrates*, J. Phys. Condens. Matter **30**, 354003 (2018).

CHAPTER 3

Conclusion and Prospects

3.1 Concluding Remarks

In conclusion, we have shown that $CoCp_2$ attached to the STM tip polarizes the spin of the tunneling current. A hybrid Kondo resonance spin excitation mode also emerges in the $NiCp_2$-$CoCp_2$ system. The hybrid mode has a Fano-Frota line shape like the Kondo resonance with the excitation energy equaling the sum of the $NiCp_2$ spin excitation and the $CoCp_2$ Kondo resonance.

3.2 Future Prospects

Previous works have also shown that coupling between a single molecule's Kondo resonance and vibrational modes produces satellite peaks [1–3]. The rules governing the coupling between the Kondo resonance and individual vibration modes have not yet been determined. Further investigations into what vibration modes can interact with the Kondo resonance in a single molecule may shed light on the nature of the coupling mechanism. It is also possible that this mechanism will allow for the investigation of vibrational overtones or other inelastic excitations thought to be inaccessible by STM-IETS.

References

[1] D. Rakhmilevitch, R. Korytár, A. Bagrets, F. Evers, and O. Tal, *Electron-Vibration Interaction in the Presence of a Switchable Kondo Resonance Realized in a Molecular Junction*, Phys. Rev. Lett. **113**, 236603 (2014).

[2] P. Roura-Bas, L. Tosi, and A. A. Aligia, *Replicas of the Kondo Peak Due to Electron-Vibration Interaction in Molecular Transport Properties*, Phys. Rev. B **93**, 115139 (2016).

[3] J. J. Parks, A. R. Champagne, G. R. Hutchison, S. Flores-Torres, H. D. Abruña, and D. C. Ralph, *Tuning the Kondo Effect with a Mechanically Controllable Break Junction*, Phys. Rev. Lett. **99**, 026601 (2007).

APPENDIX A

DSP Update

A.1 Hardware Setup

The goal of this project is to provide a replacement platform for the digital signal processor (DSP) in the STM electronics. The current DSP board we are using is the Freescale DSP 56309 EVM. While this board is reliable and suits our purposes, it is obsolete with used boards being difficult to find and are expensive when they can be found. The board also requires that the source code be written in a Motorola proprietary language similar to Assembly, which makes the code difficult to update and modify.

The replacement board we are using is the Texas Instruments (TI) LAUNCHXL-F28379D. This board is relatively inexpensive compared to the Freescale board and is still available from the manufacturer. The TI board also has more on-board memory and a faster processor than the Freescale board as well as built in ADC/DAC capability. We are not taking advantage of this built-in functionality for now to make this replacement board easy to install into the current electronics system. Additionally, the development environment for the TI board can compile using C++ instead of Assembly, allowing for easier modification to the DSP software when needed.

We also require a pin breakout board to serve as an adapter between the electronics already in use and the new DSP board. Since the pin arrangement of the Freescale board and the TI board is different, this adapter board is designed to convert the connection of the TI board to mimic the connection of the Freescale board. By using this adapter board, the new DSP will be a simple drop-in replacement, using all the same cables as the old DSP.

The DSP uses separate data and 12-bit control pin connectors to send output voltages to the scanner piezos. The only channel that does not use these connections is the sample bias which is controlled by the 20-bit DAC. The data cable is a 2x10 pin ribbon cable with 8 pins used for input signals, 8 for output signals, 1 to establish a common ground, and 3 unused. The 12-bit cable is a 1x6 pin ribbon cable with 2 pins used for the output control bits, 3 for input control bits and 1 not connected. The layout of these pins is described in detail in a figure later in this chapter.

The first and second pins of the 12-bit connector are for the control bits that govern the output signal from the DSP to the DAC boards. Since the DSP only outputs 8 bits at a time for a 12-bit number, the on state of the first pin indicates that the most significant bits (MSBs) are being sent while the off state shows that the lowest significant bits (LSBs) are being sent. The second pin of the connector acts as a latch signal, meaning that the summing board will only accept new data if it receives the confirmation signal through the second pin. As we are sending 16 bits for a 12-bit DAC, we use the 4 MSBs of the output signal to act as channel selection bits. Pins 4, 5, and 6 of the connector manage the input signal from the ADC boards to the DSP. Pins 4 and 5 act as channel selection pins while pin 6 indicates if the received byte is the MSBs or the LSBs. Since pins 4 and 5 are acting as the channel selection bits, the DSP recognizes the full 16-bit signal as the reading from the chosen channel.

The 20-bit connection is a serial connection that uses only four pins to communicate with both DAC boards of the 20-bit DAC. The serial communication is set up similarly to a Serial Peripheral Interface (SPI) connection. However, the DSP uses the data receiving pin as a second transmission pin to allow the DSP to send independent data packets to each board of the 20-bit DAC. The first pin acts as the clock, the second and third send the data, least significant bits

first, to the lower and upper registers of the 20-bit DAC respectively. The fourth pin acts as a latch, with it being off to indicate that new data is incoming. The fifth and sixth pins are not used. These six pins are wired to the first six pins of a Dsub-9 connector with the eighth and ninth pin of the Dsub-9 connector connected a +9V and ground terminals respectively of the power supply tied to the ground of the opto-isolator. The seventh pin of the Dsub-9 connector is left empty.

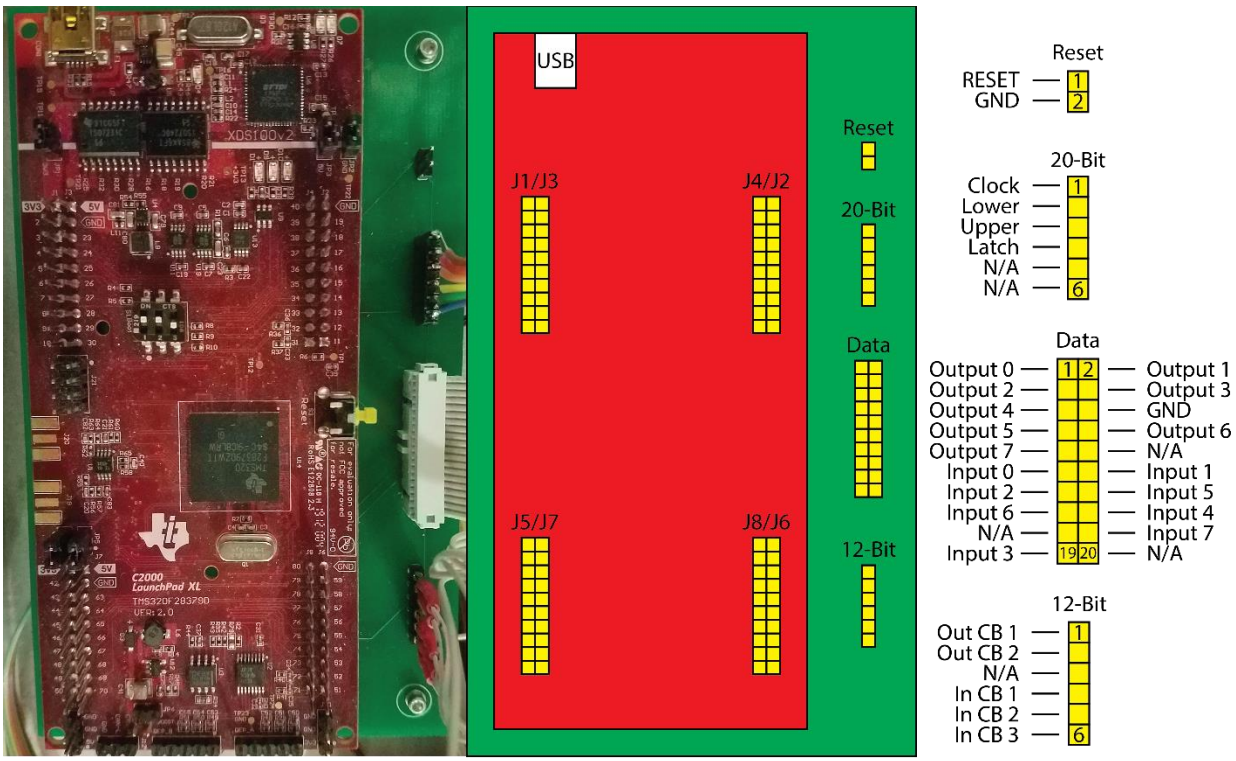

Figure A.1 TI LAUNCHXL-F28379D Board with Adapter

(A) Picture of assembled LAUNCHXL-F28379D board with adapter ready for use in a 20-Bit STM electronics system. (B) Schematic of connections from the board to electronics. The 20-Bit serial connection goes to the 20-Bit DAC. The Data and 12-Bit connections go to the computer interface used for 12-Bit parallel communication. The Data connection sends and receives the data bits while the 12-Bit connection handles the timing of the communication protocol used. (C) Labels for each pin position on the adapter board.

Table A.1 Pin Numbers, GPIO Numbers, and Breakout Pin Numbers

Breakout Pin Number	GPIO	TI Board Pin Number	Breakout Pin Number	GPIO	TI Board Pin Number
Data					
1	0	40	11	8	78
2	1	39	12	9	77
3	2	38	13	10	76
4	3	37	14	25	51
5	4	36	15	26	53
6	GND	22	16	24	34
7	5	35	17	N/A	N/A
8	6	80	18	27	52
9	7	79	19	11	75
10	N/A	N/A	20	N/A	N/A
12-Bit					
1	15	73	4	16	33
2	64	54	5	14	74
3	18	4	6	63	55
20-Bit					
1	61	19	4	58	15
2	123	18	5	59	14
3	122	17	6	124	13

A.2 Software Setup

For the current generation of Texas Instruments development kits, Code Composer Studio (CCS) is the preferred development environment. CCS is available on the TI website and is regularly updated with new features and support for newer processors. During this project, CCS has been updated several times, but each version has been compatible with the previous work. While the program does not show any signs of becoming obsolete any time soon, the open-source development environment Energia can also be made compatible with the TI board we are using.

The LaunchXL board belongs to the C2000 family of devices, so to get the software library for this board, we must download the C2000Ware software package either through the CCS software or directly from the TI website. While the compiler is specific to the family of devices, the code is not. The C2000 compiler uses standard C/C++ language, so the code can be easily ported for use on another device. However, the standard libraries that are being used for GPIO control will need to be changed if a device from another family is used. Specifically, the pin initialization and analog and serial communication functions will need to be modified if another board is used.

Memory usage and allocation is critical when working with a board with limited memory capacity compared to most computers. For large spectroscopy passes or scans, the DSP must be able to store thousands of bytes at a time before sending them through the serial connection to the STM software on the computer. However, the default memory allocated to such variables only holds 10 kilobytes. Since the current version of the STM software expects the memory to be sent in large chunks, we needed to adjust the size of the space where these data are stored.

Both the spectroscopy and scan functions store data temporarily in a global unsigned integer array. Therefore, we must expand the space allotted for global variables. Memory allocation is determined at the time of code compilation by a file referred to as a linker file. We can adjust the location and size of each space by modifying the linker file directly. For our purposes, we assigned additional empty locations to the ".ebss" space, which is where all the global variables are stored in memory. With the linker file modified, the DSP now allocates 30 kilobytes for storing scan and spectroscopy data and can handle larger scans and passes without memory errors.

Default Linker Command Code

```
41  PAGE 1 : /* Data Memory */
42           /* Memory (RAM/FLASH) blocks can be moved to PAGE0
43
44     BOOT_RSVD       : origin = 0x000002, length = 0x000121
45     RAMM1           : origin = 0x000400, length = 0x0003F8
46  //   RAMM1_RSVD      : origin = 0x0007F8, length = 0x000008
47     RAMD1           : origin = 0x00B800, length = 0x000800
48
49     RAMLS5      : origin = 0x00A800, length = 0x000800
50
51     RAMGS0      : origin = 0x00C000, length = 0x001000
52     RAMGS1      : origin = 0x00D000, length = 0x001000
53     RAMGS2      : origin = 0x00E000, length = 0x001000
54     RAMGS3      : origin = 0x00F000, length = 0x001000
55     RAMGS4      : origin = 0x010000, length = 0x001000
56     RAMGS5      : origin = 0x011000, length = 0x001000
57     RAMGS6      : origin = 0x012000, length = 0x001000
58     RAMGS7      : origin = 0x013000, length = 0x001000
59     RAMGS8      : origin = 0x014000, length = 0x001000
60     RAMGS9      : origin = 0x015000, length = 0x001000
61     RAMGS10     : origin = 0x016000, length = 0x001000
62
63  //   RAMGS11     : origin = 0x017000, length = 0x000FF8   /
64
65  //   RAMGS11_RSVD : origin = 0x017FF8, length = 0x000008
```

```
75  SECTIONS
76  {
77     /* Allocate program areas: */
78     .cinit              : > FLASHB      PAGE = 0, ALIGN(8)
79     .text               : >> FLASHB | FLASHC | FLASHD | FLASHE
80     codestart           : > BEGIN       PAGE = 0, ALIGN(8)
81     /* Allocate uninitalized data sections: */
82     .stack              : > RAMM1       PAGE = 1
83     .switch             : > FLASHB      PAGE = 0, ALIGN(8)
84     .reset              : > RESET,      PAGE = 0, TYPE = DSECT /* n
85
86  #if defined(__TI_EABI__)
87     .init_array         : > FLASHB,       PAGE = 0,       ALIGN(8)
88     .bss                : > RAMLS5,       PAGE = 1
89     .bss:output         : > RAMLS3,       PAGE = 0
90     .bss:cio            : > RAMLS5,       PAGE = 1
91     .data               : > RAMLS5,       PAGE = 1
92     .sysmem             : > RAMLS5,       PAGE = 1
93     /* Initalized sections go in Flash */
94     .const              : > FLASHF,       PAGE = 0,       ALIGN(8)
95  #else
96     .pinit              : > FLASHB,       PAGE = 0,       ALIGN(8)
97     .ebss               : >> RAMLS5 | RAMGS0 | RAMGS1,    PAGE = 1
98     .esysmem            : > RAMLS5,       PAGE = 1
99     .cio                : > RAMLS5,       PAGE = 1
100    /* Initalized sections go in Flash */
101    .econst             : >> FLASHF       PAGE = 0, ALIGN(8)
102 #endif
```

Modified Linker Command Code

```
36  PAGE 1 : /* Data Memory */
37           /* Memory (RAM/FLASH) blocks can be moved to PAGE0 for
38
39     BOOT_RSVD       : origin = 0x000002, length = 0x000120     /*
40     RAMM1           : origin = 0x000400, length = 0x000400     /*
41     RAMD1           : origin = 0x00B800, length = 0x000800
42
43     RAMLS5      : origin = 0x00A800, length = 0x000800
44
45     RAMGS0      : origin = 0x00C000, length = 0x001000
46     RAMGS1      : origin = 0x00D000, length = 0x001000
47     RAMGS2      : origin = 0x00E000, length = 0x001000
48     RAMGS3      : origin = 0x00F000, length = 0x001000
49     RAMGS4      : origin = 0x010000, length = 0x001000
50     RAMGS5      : origin = 0x011000, length = 0x001000
51  //   RAMGS6      : origin = 0x012000, length = 0x001000
52  //   RAMGS7      : origin = 0x013000, length = 0x001000
53  //   RAMGS8      : origin = 0x014000, length = 0x001000
54     RAMGS6      : origin = 0x012000, length = 0x003000
55     RAMGS9      : origin = 0x015000, length = 0x003000
56  //   RAMGS10     : origin = 0x016000, length = 0x001000
57  //   RAMGS11     : origin = 0x017000, length = 0x001000
58     RAMGS12     : origin = 0x018000, length = 0x001000     /* Onl
59     RAMGS13     : origin = 0x019000, length = 0x001000     /* Onl
60
61     CPU2TOCPU1RAM   : origin = 0x03F800, length = 0x000400
62     CPU1TOCPU2RAM   : origin = 0x03FC00, length = 0x000400
63  }
```

```
65  SECTIONS
66  {
67     /* Allocate program areas: */
68     .cinit              : > FLASHB      PAGE = 0, ALIGN(4)
69     .text               : >> FLASHB | FLASHC | FLASHD | FLASHE
70     codestart           : > BEGIN       PAGE = 0, ALIGN(4)
71     /* Allocate uninitalized data sections: */
72     .stack              : > RAMM1       PAGE = 1
73     .switch             : > FLASHB      PAGE = 0, ALIGN(4)
74     .reset              : > RESET,      PAGE = 0, TYPE = DSECT /*
75
76  #if defined(__TI_EABI__)
77     .init_array         : > FLASHB,       PAGE = 0,       ALIGN(4
78     .bss                : > RAMLS5,       PAGE = 1
79     .bss:output         : > RAMLS3,       PAGE = 0
80     .bss:cio            : > RAMLS5,       PAGE = 1
81     .data               : > RAMLS5,       PAGE = 1
82     .sysmem             : > RAMLS5,       PAGE = 1
83     /* Initalized sections go in Flash */
84     .const              : > FLASHF,       PAGE = 0,       ALIGN(4
85  #else
86     .pinit              : > FLASHB,       PAGE = 0,       ALIGN(4
87  //    .ebss               : >> RAMLS5 | RAMGS0 | RAMGS1,    PAGE
88     .ebss               : >> RAMLS5 | RAMGS9 | RAMGS1,    PAGE =
89  //    .esysmem            : > RAMLS5,       PAGE = 1
90     .esysmem            : > RAMGS6,       PAGE = 1
91     .cio                : > RAMLS5,       PAGE = 1
92     /* Initalized sections go in Flash */
```

Figure A.2 Modifications to Linker File

Highlighted sections identify the memory sections that are changed to accommodate the large number of data points stored for spectroscopy passes and scan lines. The original file has several sections split into smaller sections that cannot hold the stored data. The modified file combines these sections into a single large space.

The DSP board can be updated by any computer that has a USB port and CCS with the C2000 software installed. To begin, create a new CCS project and change the target platform to the appropriate device. In our case, the target should be the TMS320F28379D microcontroller connected through a Texas Instruments XDS100v2 USB debug probe. If everything is working properly, the program should recognize that the device is a member of the C2000 family and change the compiler to a functioning version. Since all the source files needed are stored in the archive file, begin with an empty project so that there will be no duplicate files to create confusion.

With the target version of the software extracted from the archive file, copy the source code (*.c and *.asm) files into the project folder. All the relevant files are either in the root folder or in the Functions or Headers folders. If the Functions and Headers folders are copied over into the project, they must be included in the file search paths specified in the compiler options for the new project. Additionally, the source code references common libraries included in the C2000 software package. These libraries must also be included in the file search paths for the compiler to function properly. Since the microcontroller we are using is a dual core processor, we must also pre-define the symbol “CPU1” as a sign that we are using that processor for this program. Finally, the linker file used by the program must be modified as explained in the previous section. Once these changes are made, the program is ready to be built and pushed to the DSP board.

Code Composer Studio has three different options for compiling projects: building, debugging, and loading. Building the project is the quickest option as it compiles the program without pushing it to the target board. Building is useful for making sure that there are no obvious, critical errors with the code before making changes to the board. Debugging also builds

the project, but it requires a working connection with the board. After building the project, CCS will load it to the board and launch a debugging session that can be used to test different functions of the DSP code. The debugging session is somewhat limited for our purposes as we require a dedicated serial communication port to send commands and receive data from the DSP board to test new functions. Finally, CCS can load the project onto either the flash or ram memory on the board. Loading the project to ram memory is faster, but the program will be erased when the board is unplugged from its power source. Since we need to make sure that the program will remain on the board even after the electronics are turned off, it is best to load the project into the board's flash memory.

CCS also has the option of optimizing code during compile, but this step is unnecessary and potentially harmful for the DSP program. Many functions that we use have built in delays due to the electronics hardware, so improving the speed of the program is not helpful. However, optimization can also adjust how data is stored in memory on the board. Several functions in the program need the memory to be carefully managed to correctly process the command sent by the STM computer software. Therefore, we do not use any automated code optimization when building this project.

The main structure of the STM DSP firmware is a switch statement with each function that can be called given a unique command character. Once the DSP receives a valid command character, it waits for several bytes specific to the called function that represent parameters needed. With the parameters received, the DSP launches into the called function until completion or a stop command is received. When the function is complete, the DSP returns to the main loop and waits for the next command character from the STM software. To introduce a

new function into the DSP code, a new command character and the number of bytes sent as parameters must be included in the main header file.

The DSP functions are grouped with the subroutines that they need. For example, the analog output function contains not only the function called from the main loop of the program, but also the generalized output function is used for any 12-bit output to the electronics. Most files also pair the setup functions used for each primary function, such as ScanSetup and ScanLine. Since the setup function and the primary function are not always called together, the setup functions save the relevant parameters as global variables for future use.

To build a new function into the DSP firmware, create a new source file in the Functions folder named for the new function about to be included. In addition to any library headers needed for the function, make sure to include the DSP_FUNCTIONS.h file so that the new function can access any global variables and other functions available. Once the new source file is ready, the DSP_FUNCTIONS.h file must also be modified to include any new global variables and function declarations. A unique command character and the total number of bytes for incoming parameters must also be defined in the header file to allow the new function to be included in the main loop of the DSP program. Once the header file is modified, the new function can be included in the two switch statements in the main.c loop, the first to accept the parameters byte by byte and the second to call the new function.

Table A.2 Current Command Characters

Function	Command Character	Function	Command Character
Analog Output	o	Ramp	r
Analog Input	i	Ramp and Read	R
16-Bit Analog Output	H	Ramp Diagonal Setup	l
20-bit Analog Output	X	Ramp Diagonal	L
Autoplus	-	Read Sequence Setup	Q
Autominus	+	Scan Line Setup	s
Debug Get	b	Scan Line	S
Debug Set	B	Spectroscopy Setup	y
Delay	d	Spectroscopy	Y
Deposition Setup	p	Square Wave	q
Deposition	P	Tip Approach Setup	t
20-bit Deposition Setup	u	Tip Approach	T
20-bit Deposition	U	Translate Sample	a
Giant Step	g	Track Setup	k
Hop Setup	j	Track	K
Hop	J	Version	v

A.3 STM Function Descriptions

The latest version of the DSP firmware has a total of 32 different functions that can be called by the STM computer software. Most of these functions are self-explanatory, but there are a few that require clarification.

The main use of the deposition function is to change the apex of the STM tip with a combination of a voltage pulse and bringing the tip into contact with the surface. The function is called deposition because after a successful "poke," the tip deposits a small amount of metal onto the surface from the apex of the tip. Each deposition begins by saving the tunneling parameters used before starting so that the tip can be returned to its original position. Then the feedback circuit is set according to the sent parameter and the Z offset value is stepped, not ramped, to the new value. If the feedback circuit is left on, it will begin compensating for the sudden change, pulling the tip back away from the surface, but more commonly the feedback loop is opened for the duration of the poke. After Z offset is adjusted, the sample bias and tunneling current setpoints are also stepped or ramped to new values. Here, there is the option to slowly ramp these channels, with the slope given by the "wait" delay parameter. If the feedback circuit is open during the poke, the tunneling current setpoint will have no effect on the position of the tip until feedback is restored.

Once the Z offset, sample bias, and tunneling current setpoints have all been changed, the DSP will either read from a specified channel for a given number of points and averaging so many samples for each point, or it will simply wait for an equivalent amount of time. These readings are not used in practice, but they can be used to tell exactly when the tip changes by recording the tunneling current and observing when there is a change in the conductance. This step can be modified to implement an automated tip fixing algorithm. In the older versions of

this function, there was also the option to extend the duration of the poke until the tunneling current changed a certain number of times. However, this feature can cause the DSP to be caught in an infinite loop if the tip is too stable at the deposition setpoints, so it has been removed in this version of the firmware.

Once the reading or waiting is done, deposition finishes by restoring the original setpoint conditions. First, it steps Z offset to the previous value, then the bias and tunneling current, and finally the feedback circuit setting. If there has been a change in the tip, the feedback circuit will adjust the Z feedback channel to match the tunneling current setpoint. Therefore, after a successful deposition, the STM will see a change in the Z feedback channel and most likely a small new protrusion on the surface at the position the tip was in. Finally, if any data was read during the poke, the DSP will send it to the computer to be displayed and saved.

Tip approach is used to bring the STM tip into tunneling distance of the sample. In our Besocke-style scanner, this means that the outer piezo tubes work together to move in a rhythmic, stick-slip motion to move down the ramps of the sample holder to bring the sample down towards the tip. The loop of this function is split into two steps, coarse approach and tunneling current check, also known as the giant steps and the baby step.

The loop starts by checking the tunneling current before moving the sample closer to the tip. The outer piezo tubes move during this step, starting at a neutral position and retracting to bring the surface closer to the tip while reading the tunneling current channel. Baby step size is the number of bits that the outer piezo voltage increases before reading the tunneling current. If the measured value from the tunneling current input channel is greater than the minimum tunneling current set at the beginning of the approach, the loop will stop and send the value of the piezo tube position back to the computer. Otherwise, the outer piezo tubes are restored to a

neutral position using a nonlinear ramping motion to move the sample back into position quickly but smoothly to prevent the sample from moving during the baby step.

If the minimum tunneling current is not seen during the baby step, the coarse approach step begins. The loop makes the given number of giant steps before checking for a stop command from the computer in case the loop needs to be ended early. Each giant step can be broken down into four parts. First, the outer piezos move along the sample holder ramp up to the X outer step size. This X outer motion is also nonlinear, moving faster at the end of the ramp. Immediately after this ramp is complete, the piezos drop away from the sample, stepping the Z outer channel to Z outer step size voltage. The DSP will wait 15 microseconds before stepping the X outer channel back to its original position. After these quick movements, the DSP will delay the specified number of milliseconds before restoring the piezos back to its original position, using the same nonlinear ramp used in the baby step. Once all the giant steps of the loop are complete, the DSP will measure the tunneling current and send the value back to the computer.

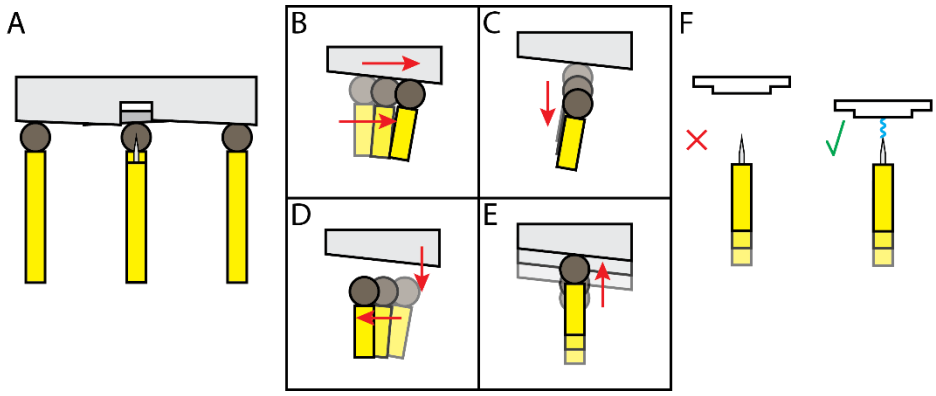

Figure A.3 Schematic of the Tip Approach Procedure.

A) Side view of a Besocke-style STM scanner. Three tungsten ball tipped piezo tubes support the sample holder above the STM tip. B-E) Diagrams of the four main steps of the course approach step called the giant step, moving the surface closer to the tip. The outer piezo tubes move together in a stick-slip motion to steadily move down the sample holder ramp to bring the surface closer to the STM tip. F) Diagram of the tunneling check step called the baby step. The center piezo tube holding the STM tip advances to its limit, checking the tunneling current until it reads a pre-determined minimum value.

Scanline is one of the most called functions in normal operation of the DSP. Each image is centered at a point determined by the X and Y offset channels and is read line by line in a raster scan pattern using the X and Y fine control channels. The size of the scan is the product of the total number of points to be read, the number of steps in between each point, and the gain settings for the fine control channels. For example, the size of a scan with 128 points on a side, 4 steps between points and a gain of 1 is $128\ steps\ \times 4\frac{bits}{step}\ \times\ \frac{+10V-(-10V)}{2^{12}\ bits} \times 1 = 2.5\ V$. To convert this voltage to a physical distance, the piezoelectric response of the center piezo tube must be included. However, this response is temperature dependent so in practice, an image of the crystal lattice of the surface is used to calibrate the size of the scan.

Along with the size of the scan, the three delay parameters and the reading times determine the time each scan takes to complete. Interstep delay is the amount of time the DSP waits in between each step when moving to the next point in the line. The read delay is built into the read sequence as the extra time to wait for the tip to settle before reading. The interline delay is not integrated into the scanline function, but it is the delay time before the next scanline is called over the course of scanning an image. Finally, an individual read of any analog channel needs approximately 25 μs but reading accounts for most of the time needed for a scan when multiplied by the total number of points to read over the course of an image.

Since scanline takes so much time, it is important to compensate for thermal drift especially with the feedback circuit. The feedback circuit has a limited output range, so if the tip drifts too much, it can pull out of tunneling range or crash into the surface. Included in scanline is a check against drift called scan protection. If the tunneling current ever deviates from the setpoint by a set percentage, one of four crash protections activate. The most used crash protection is to call the autominus function in the middle of the scan, which gives the feedback

circuit a larger range of voltages to work with. The other options are to do nothing about the crash, to stop the scan completely, or to call a modified version of the autominus function that does not adjust the z offset channel as much as the unmodified function.

The last three parameters that scanline needs determine the direction the tip moves during the scan. The output channel is the channel that is stepped through for each line. The direction bit tells the DSP if tip is moving forward or backward and the read bit is whether or not the DSP reads while moving through the line. Scanline is always called forward and backward, but the read bit determines if the image(s) sent to the computer are read forward and/or backward.

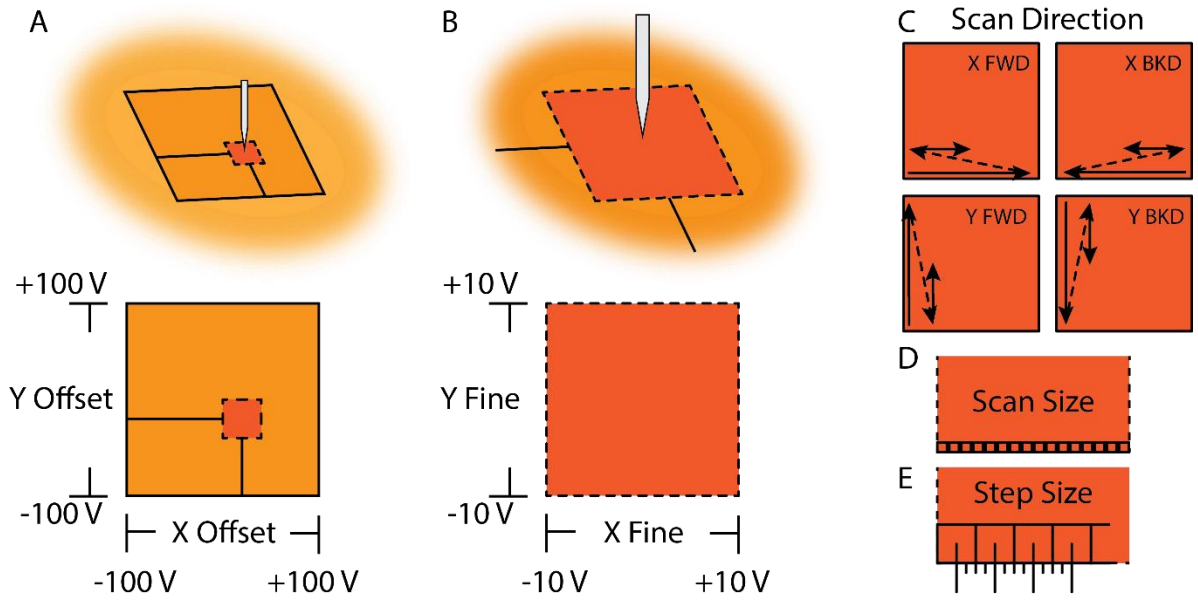

Figure A.4 Schematic Outlining Parameters for the Scanline Function.

A) The scanning region available to the STM is constrained by the maximum output voltage on the X and Y offset channels. The offset channels determine the center of the scan box and are limited to +/-100V. B) The size of any individual scan is constrained by the X and Y fine control channels. At gain 1, the X and Y fine control channels are limited to a maximum of +/-10V. The position of the tip is determined by the sum of the offset and fine control output voltages. C) Schematics of the four scan direction options. D) The scan size parameter determines the number of points measured in each line and the number of lines in the scan. Shown is a scan size of 16. E) The step size parameter determines the distance in bits between each point in the scan. Shown is a step size of 4.

Spectroscopy can be summarized as two bias channel ramps from the range minimum to the maximum and back to the minimum while reading from the input channels. The step size parameter controls the distance between each point being read in the ramp and the forward and backward flags determine if reading during each pass is requested. There is also an option to change the output channel but in practice this only allows the DSP to control the resolution of the output bias without modifying the software. The output channel is 20 for a 20-bit DAC system, 10 for a 16-bit DAC system and 0 for a 12-bit DAC.

When spectroscopy is started from the STM software, the DSP starts with a ramp to change the bias from the current setpoint down to the minimum to start the spectroscopy function without a sudden change in sample bias. The speed of the initial ramp is determined by the ramp delay parameter. The step delay time controls the speed of the ramp between bias values during the spectroscopy pass while the read delay is the amount of time the DSP waits for the lock-in amplifier to settle on a new value before the DSP reads from each channel. Step and ramp delays can be very short, but the read delay must be at least 3x the lock-in amplifier time constant to have an accurate reading.

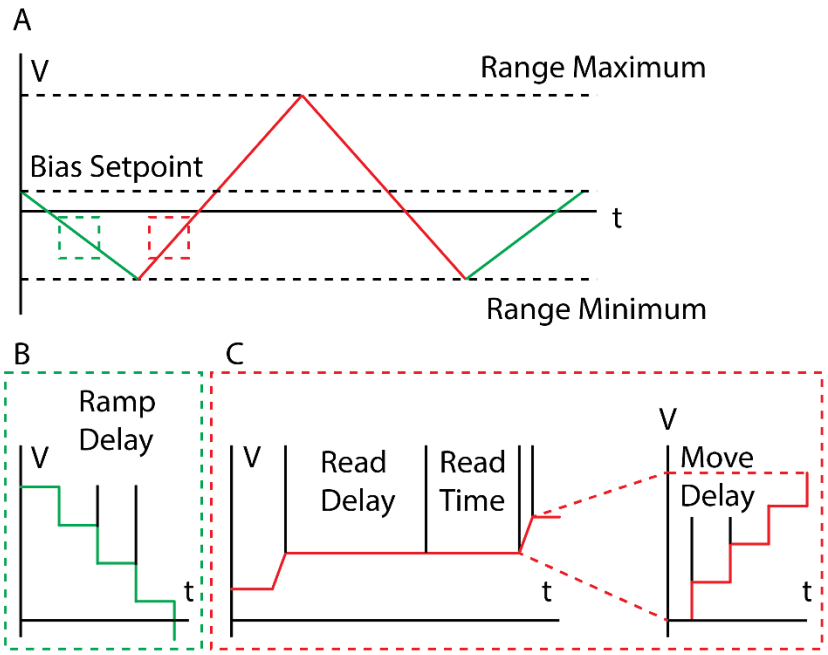

Figure A.5 Example Output Waveform for a Spectroscopy Pass.

A) One spectroscopy pass can be split into four steps: ramp from initial bias to lower end of range, forward pass reading while ramping from bias minimum to maximum, backward pass ramping from maximum to minimum, and ramp restoring bias to original setpoint. B) Starting and restoring bias ramps are done by calling the ramp function. The slope of these ramps is determined by the ramp delay parameter. C) Forward and backward passes are combined in the Spectroscopy function. Read delay is needed to allow the lock-in amplifier value to settle before reading each input channel. Move delay determines the speed of the ramp to each new bias value.

The goal of the autoplus and autominus functions is to return the z feedback output to zero by adjusting the Z offset channel. Once within tunneling range, the distance from the sample to the tip is determined by the sum of the voltages applied by the Z offset channel and the Z feedback circuit. With the feedback circuit closed, the sum of these voltages is held constant to maintain a constant tunneling current. When autoplus or autominus is called, the Z feedback voltage is read, and Z offset is incremented bit by bit until the Z feedback voltage changes polarity. At this point, autoplus will adjust Z offset to make sure that Z feedback is slightly positive, while auto minus will make Z feedback slightly negative.

The track function maintains the tip position over a local maximum or minimum on the surface. Starting at a position given by the STM software, this function will read the Z feedback channel at the origin point, its nearest neighbors, and next nearest neighbors in a 3x3 grid. The DSP will use the plane fit parameters to adjust each point's value to correct for any plane tilt of the sample. When tracking the local maximum (minimum), the x and y coordinates of the position with the highest (lowest) value will be sent back to the STM software. After sending these coordinates, the DSP will wait for a command character from the computer either to continue tracking with the new best position without needing any new parameters to be sent along, or to stop tracking and return to the main loop of the program.

Hop tracking works differently than the usual tracking function. First, instead of checking the nearest neighbors around the starting position, the DSP receives two parameters to establish a radial distance around the starting point. Second, hop calculates a gradient around the center point and returns two integers representing the slopes in the x and y directions as well as the total time required to calculate the gradient. After the first loop is complete, it waits for one of two commands from the STM software, either to continue or to stop. If it does continue, the

STM software also sends a new center point to move to and calculate a new gradient. A major difference between hop and track is that hop requires the STM software to reposition the tip after each loop while track handles all repositioning without any new information from the computer.

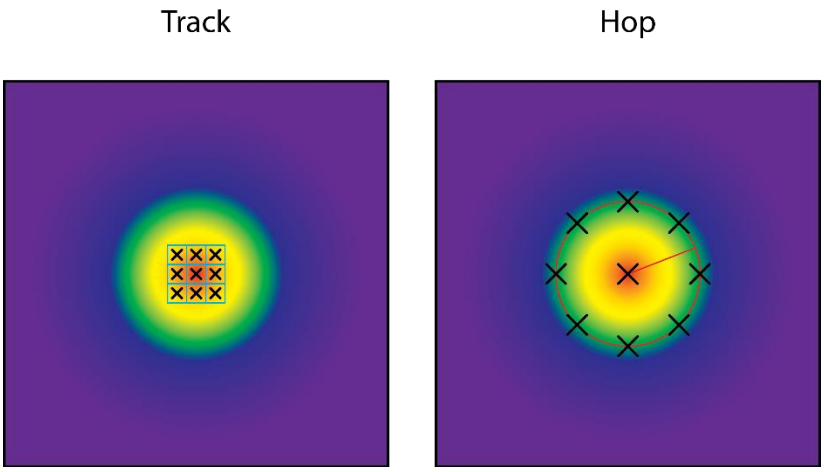

Figure A.6 The Difference Between Track and Hop Tracking.

Standard tracking compares the z feedback value of the start point and the 8 nearest neighbors and moves the tip to the position with the highest (lowest) value if tracking the maximum (minimum). Hop tracking defines the distance of the points to be read from the starting point. The gradient is calculated from these points and is sent to the computer to find the new best position to move the tip to.

A.4 Further Improvements

During a scan or a spectroscopy pass, reading from an analog channel follows the same pattern no matter which channel is read. Before starting to read, we have a built-in delay time to allow the system to stabilize after the previous change whether that means that the piezo tubes need time to settle after moving, or the lock-in amplifier accumulates enough signal to give an accurate reading. This delay time varies from channel to channel, ranging from less than 1 ms for reading I or Z to 400ms for reading from the lock-in channel. These delays account for a large portion of the time that it takes for a scan or spectroscopy pass to complete. Much of the remaining time spent to complete a scan is taken up by reading from the ADC.

The ADC chip that we use now has a sampling rate of 50 kHz, meaning that whenever it reads from the analog channels, it requires a minimum of 20 μs to complete a single read. This time is not significant until it is multiplied by the hundreds or thousands for each point in a scan or spectroscopy pass. For example, our standard for an itProbe scan is to wait 400 ms then read approximately 16000 times total from the different analog channels, giving us an estimated time of 720 ms per pixel in the image. For a small 64x64 pixel image, this adds up to 2949 seconds ≈ 49 minutes. The measured time for the same image is 3732 seconds, meaning that the remaining 13 minutes is used for ramping the piezo voltages and any processing time needed for the averaging.

To improve these times, the current ADC chip could be upgraded to have a faster sampling rate. A commercially available 16-bit ADC with 1MHz sampling rate would reduce the time needed for the above itProbe image by approximately 20 minutes by shortening the conversion time needed to read the analog signal from 20 μs to 1 μs. See the table below for other estimated improvements on the performance of the electronics. While the improvement to

spectroscopy times is negligible, the speed increase to most scanning sequences may make this upgrade to the electronics worthwhile. To make this change, the electronics system would need to be redesigned, though only the ADC card and a small portion of the DSP code would need to be changed. Currently, the 20 μs conversion time is hard coded into the analog read function and would need to be modified to be compatible with a faster ADC chip.

Table A.3 Estimated Speed Improvements from ADC Upgrade

Operation	Unmodified Total Time	Unmodified Conversion Time	Modified Conversion Time	Change in Conversion Time	Modified Total Time	Speed Increase
Topography Scan 128x128x8x1 377 Avg 237 µs read delay	254 seconds	123.5 seconds	6.2 seconds	-117.4 seconds	136.6 seconds	+85.9%
itProbe Scan 64x64x8x0.1 16000 Avg 400 ms read delay	3732 seconds	1310.7 seconds	65.5 seconds	-1245.2 seconds	2486.8 seconds	+50.0%
Spectra Pass 200 points 1000 Avg 400 ms read delay	210 seconds	24 seconds	1.2 seconds	-22.8 seconds	187.2 seconds	+12.2%

By extending the memory for stored data, the DSP functions for all but the largest scan sizes. However, this is only a quick fix for the root problem of memory storage. For the DSP to function properly for all scan and spectroscopy pass sizes, it needs to send the data in smaller chunks. By sending the data piecemeal instead of as one large chunk, we can greatly reduce the overall storage requirements of the DSP. The tradeoff for better memory efficiency is more time spent with serial communication. In the extreme case, after measuring each point the result is sent to the STM software before the next point is measured. Normally, this would increase the overall time that a scan or spectroscopy pass would need to complete, but we have a built-in interstep delay in our software. During the time that the DSP waits in between points to allow the tip to stabilize after stopping, the DSP can send the recently read data to the STM software. By reducing the interstep delay time and instead using some time before reading to send the most recently measured data, we can achieve better memory efficiency and maintain our current scan speeds.

The downside to this change in the scanning and spectroscopy functions is that it also requires the STM software to change. The STM software would need to be updated to allow for the increased serial communication during a scan or spectroscopy pass. As this project is focused on creating a device that is compatible with our current software and hardware, this change has not been implemented, but it is recommended that this update be considered in future updates to the STM software.